Haobo Hua
Department of Mathematics,
Korea University,
Seoul 136-713, China;
Department of Mathematics and Physics,
Zhengzhou Institute of Aeronautical
Industry Management,
Zhengzhou 450015, China
e-mail: huahbo@korea.ac.kr

Jaemin Shin
e-mail: zmshin@korea.ac.kr

Junseok Kim[1]
e-mail: cfdkim@korea.ac.kr

Department of Mathematics,
Korea University,
Seoul 136-713, China

Level Set, Phase-Field, and Immersed Boundary Methods for Two-Phase Fluid Flows

In this paper, we review and compare the level set, phase-field, and immersed boundary methods for incompressible two-phase flows. The models are based on modified Navier–Stokes and interface evolution equations. We present the basic concepts behind these approaches and discuss the advantages and disadvantages of each method. We also present numerical solutions of the three methods and perform characteristic numerical experiments for two-phase fluid flows. [DOI: 10.1115/1.4025658]

Keywords: level set method, phase-field method, immersed boundary method, two-phase flows, surface tension, Navier–Stokes equation, computational fluid dynamics

1 Introduction

Many important industrial problems involve multiphase fluid flows [1–4]. The multiphase fluid flows are related to many physical problems, such as the non-Newtonian flow, microtube flow, droplet impact on a solid surface, and Marangoni convection. However, the modeling and simulation of multiphase flows are difficult because of the moving interfaces.

We consider two incompressible and immiscible fluids in a two-dimensional domain $\Omega = \Omega_1 \cup \Omega_2$ and define the interface as $\Gamma = \overline{\Omega}_1 \cap \overline{\Omega}_2$ (see Fig. 1). The equations governing the motion of the two fluids are the modified Navier–Stokes equations:

$$\rho\left(\frac{\partial \mathbf{u}}{\partial t} + \mathbf{u}\cdot\nabla\mathbf{u}\right) = -\nabla p + \nabla\cdot\left[\eta\left(\nabla\mathbf{u} + \nabla\mathbf{u}^T\right)\right] + \mathbf{SF} + \rho\mathbf{g} \quad (1)$$

$$\nabla\cdot\mathbf{u} = 0 \quad (2)$$

where $\mathbf{u}(\mathbf{x},t)$ is the velocity, $p(\mathbf{x},t)$ is the pressure, $\rho(\mathbf{x},t)$ is the density, $\eta(\mathbf{x},t)$ is the viscosity, $\mathbf{g}$ is the gravitational force, the superscript T denotes the transpose, $\mathbf{x} = (x,y)$ are Cartesian coordinates, and t is the time variable. The continuum surface force (CSF) model [5] is used to represent the singular surface tension force:

$$\mathbf{SF} = -\sigma\kappa\delta_\Gamma\mathbf{n} \quad (3)$$

where σ is the surface tension coefficient, κ is the mean curvature of the interface, δ_Γ is the surface δ function, and $\mathbf{n}$ is the unit normal vector to the interface from fluid 1 to fluid 2.

We focus on the review of three methods for simulating two-phase flows. The level set method (LSM) [6–35] uses a level set function to capture the interface. The phase-field method (PFM) [36–67] uses an order parameter to capture the interface, and the immersed boundary method (IBM) [68–91] uses Lagrangian marker points to track the interface. We will provide a detailed description of the basic techniques of each method.

LSM, first introduced in Ref. [6], is a popular computational technique for capturing moving interfaces (see Refs. [16,20] for reviews). For the two-phase flows, the authors in Ref. [8] first introduced a reinitialization procedure to maintain the level set function as a distance function. In this method, a smoothed δ function is used to adapt the CSF framework.

PFM is an increasingly popular method for modeling the dynamics of multiphase fluids (see Refs. [39,66] for reviews). In PFM, there is a diffuse-interface with a finite width between two phases. The density, viscosity, and other physical quantities are characterized by an order parameter, which is governed by the modified Cahn–Hilliard equation. The Cahn–Hilliard equation was first proposed by Cahn and Hilliard to describe the initial stage of spinodal decomposition [92] and it models the interface dynamics, including the surface minimization, topological changes, and phase separation.

IBM was originally developed to model the blood flow in the heart [68,69]. Since then, a number of modifications and improvements have been proposed (refer to Refs. [78,81] for reviews). The authors in Ref. [70] used the δ function to construct an indicator function to distinguish the fluid properties. The interface is also numerically diffused by the use of δ function to efficiently and conveniently distribute boundary forces.

The paper is organized as follows: 1) In Sec. 2, we present the governing equations for LSM, PFM, and IBM, 2) We summarize the formulas of surface tension force in Sec. 3, 3) We describe the treatment for the variable density and viscosity functions in Sec. 4, 4) We discuss volume conservation problems in Sec. 5, 5) In Sec. 6, we present the numerical method to solve the discrete Navier–Stokes equations and respective equations for the interface, 6) Numerical results are presented in Sec. 7, and 7) Finally, conclusions are drawn in Sec. 8.

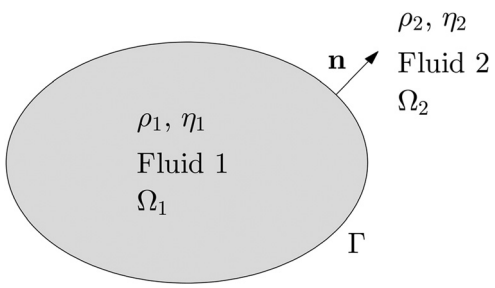

Fig. 1 Schematic of a two-phase domain

[1]Corresponding author.

Contributed by the Fluids Engineering Division of ASME for publication in the JOURNAL OF FLUIDS ENGINEERING. Manuscript received June 7, 2013; final manuscript received October 8, 2013; published online November 22, 2013. Assoc. Editor: Samuel Paolucci.

2 Governing Equations and Interface Representation

The three methods share common modified Navier–Stokes equations (1) and (2). In this section, we briefly describe the level set function, phase-field function, and Lagrangian variable for representing the interface of the two immiscible fluids. We then introduce the corresponding governing equations for evolving the interface. We also briefly discuss the advantages and disadvantages of each method.

2.1 LSM. The interface of two phases is defined implicitly using the level set function $\phi(\mathbf{x}, t)$. Here, ϕ is taken to be the signed distance from the interface Γ and it becomes the distance function satisfying $|\nabla\phi| = 1$. We take the value of ϕ to be zero at the interface Γ. Thus, ϕ has an opposite sign in each phase; see Fig. 2.

The evolution of the level set function ϕ is governed by the transport equation

$$\phi_t + \mathbf{u} \cdot \nabla\phi = 0 \tag{4}$$

During the process of interface evolution, ϕ tends to deviate from the signed distance function. However, because the density and surface tension depend on ϕ, we should maintain ϕ as the signed distance function [8,10]. Therefore, at each time step, a reinitialization step is needed to recover to the signed distance function without changing its zero level set. Specifically, taking the function ϕ at time t as an initial condition, we solve the reinitialization equation to the steady state

$$\frac{\partial d}{\partial \tau}(\mathbf{x}, \tau) = S(\phi(\mathbf{x}, t))(1 - |\nabla d(\mathbf{x}, \tau)|) \tag{5}$$

$$d(\mathbf{x}, 0) = \phi(\mathbf{x}, t) \tag{6}$$

where τ is the pseudotime and $S(\phi)$ is the sign function. For the numerical implementation, we use a smoothed sign function $S_\beta(\phi) = \phi/\sqrt{\phi^2 + \beta^2}$, where β is usually one or two grid lengths. For more details, we refer to Ref. [19]. After solving up to the steady state, $\phi(\mathbf{x}, t)$ is replaced by $d(\mathbf{x}, \tau_s)$, where τ_s is the steady-state time. There are efficient ways to solve Eqs. (5) and (6) to the steady state by using the fast marching method [11].

Advantages of LSM include the simplicity to implement, ability to capture the merging and breakup of interfaces automatically, and flexibility to describe the complex interface geometry. However, typical LSM has a lack of mass conservation. This could lead to nonphysical interface motions, which severely deteriorate the accuracy and stability of the simulation results. Therefore, many approaches have been developed to resolve the mass conservation problem for LSM, which will be described in Sec. 5.1.

2.2 PFM. In PFM, a thin finite interface is used to separate two homogeneous phases. This method uses an order parameter ϕ that is a measure of the relative composition or volume fraction of the two components. The function ϕ is distributed continuously

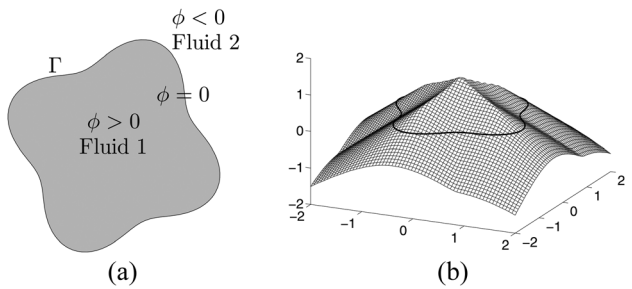

Fig. 2 (*a*) Zero contour of the signed distance function ϕ and (*b*) surface plot of ϕ with the zero contour

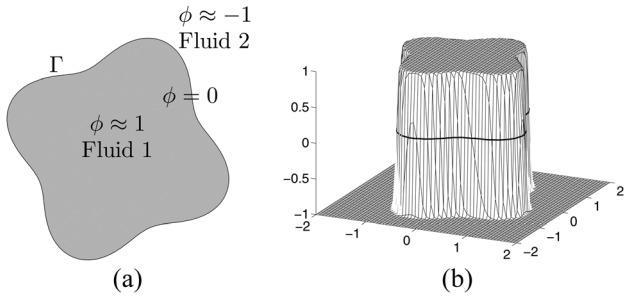

Fig. 3 (*a*) Zero contour of the order parameter ϕ and (*b*) surface plot of ϕ with the zero contour

on thin interfacial layers and uniformly in the bulk phases as shown in Fig. 3. Here, the order parameter is defined by $\phi \approx 1$ in fluid 1 and $\phi \approx -1$ in fluid 2, while the interface Γ is defined by $\phi = 0$. The sharp fluid interfaces are replaced by thin (but nonzero) thickness transition regions.

The evolution of the phase-field function ϕ is governed by the advective Cahn–Hilliard equation as follows:

$$\frac{\partial \phi}{\partial t} + \nabla \cdot (\phi \mathbf{u}) = M\Delta\mu \tag{7}$$

$$\mu = F'(\phi)^2 - \varepsilon^2\Delta\phi \tag{8}$$

where M is the constant mobility, μ is the chemical potential, $F(\phi) = (1 - \phi^2)^2/4$ is the bulk energy density that has two minima corresponding to the two stable phases of the fluid, and ε is a measure of interface thickness. It is convenient to use the dimensionless Peclet number, which is defined as $Pe = U_c L_c/M$, where U_c is the characteristic velocity and L_c is the characteristic length (refer to Ref. [52] for details).

As shown in Fig. 4, from the choice of an equilibrium profile $\phi(x) = \tanh(x/(\sqrt{2}\varepsilon))$ on the infinite domain, the concentration field varies from -0.9 to 0.9 over a distance of about $\xi = 2\sqrt{2}\varepsilon\tanh^{-1}(0.9)$ [41]. We note that $\xi = O(\varepsilon)$, and, in the sharp interface limit $\varepsilon \to 0$, the classical Navier–Stokes equations and jump conditions are recovered [39].

PFM shares the advantages of LSM. Moreover, because the order parameter has physical meanings, it can be applied to many physical phase states such as miscible, immiscible, and partially miscible ones. However, the phase-field functions change quickly near the interface and, hence, must be well resolved. In other words, a relatively large number of grid points near the interface are needed. Choosing appropriate parameter ε value is important for the accurate calculations. Taking too large ε can

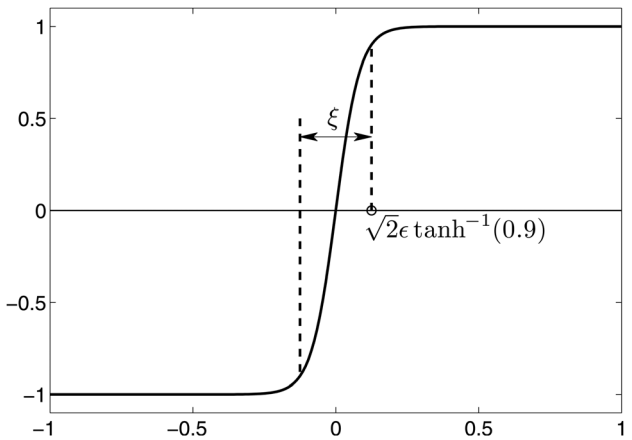

Fig. 4 Concentration profile across the diffused interface region with the thickness ξ

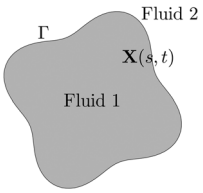

Fig. 5 Immersed boundary configuration $\mathbf{X}(s,t)$ for representing the interface Γ

make nonphysical solutions, while too small ε leads to numerical difficulties.

2.3 IBM. In IBM, the interface Γ between two fluids is described by the parametric function $\mathbf{X}(s,t)$, where $0 \le s \le L$ and L is the length of the boundary (see Fig. 5). The fluid velocity $\mathbf{u}(\mathbf{x},t)$ is an Eulerian variable, whereas the interface boundary velocity $\mathbf{U}(s,t)$ is defined at the Lagrangian variable $\mathbf{X}(s,t)$, by using the δ function and velocity $\mathbf{u}(\mathbf{x},t)$. The two-dimensional Dirac δ function $\delta^2(\mathbf{x})$ is defined by the product of one-dimensional Dirac δ functions, $\delta^2(\mathbf{x}) = \delta(x)\delta(y)$.

The evolution of the interface is governed by

$$\frac{\partial \mathbf{X}(s,t)}{\partial t} = \mathbf{U}(s,t) \tag{9}$$

$$\mathbf{U}(s,t) = \int_\Omega \mathbf{u}(\mathbf{x},t)\delta^2(\mathbf{x} - \mathbf{X}(s,t))d\mathbf{x} \tag{10}$$

First, the flow is computed in the computational domain with surface tension forces generated by the immersed boundary. The fluid reacts to the existence of the boundary via the singular force, which is spread to the surrounding Eulerian points using a discrete δ function. The immersed boundary is then advected by the fluid velocity obtained from interpolating the Eulerian points.

IBM has the principal advantage over the other two methods because it can use a large number of interfacial marker points to accurately handle the interface geometry. The major drawback is the difficulty of topological change unless the additional work for geometric problems is considered. Because the interface between two fluids moves discretely, area conservation does not, in general, hold. We will discuss the mass conservation problem for IBM in Sec. 5.3.

2.4 Multiphase and Multicomponent System. We briefly describe the multiphase and multicomponent system for each method. Let us consider N-phase fluid flows. In LSM, the motion of the interfaces is given by

$$\frac{\partial \phi_i}{\partial t} + \mathbf{u} \cdot \nabla \phi_i = 0 \quad \text{for} \quad i = 1, \ldots, N \tag{11}$$

where the separate level set function ϕ_i, which is positive in phase i and negative outside; please refer to Refs. [15,18,23] for more details. In PFM, let $\mathbf{c} = (c_1, c_2, \ldots, c_{N-1})$ be the phase variable with $c_1 + c_2 + \cdots + c_N = 1$ [66,67]. The motion of the interfaces is given by

$$\frac{\partial \mathbf{c}}{\partial t} + \nabla \cdot (\mathbf{cu}) = M\Delta\mu \tag{12}$$

$$\mu = F'(\mathbf{c}) - \varepsilon^2 \Delta\phi \tag{13}$$

In IBM, the evolution of the interface is governed by

$$\frac{d\mathbf{X}_i}{dt} = \mathbf{U}_i \tag{14}$$

where $\mathbf{X}_i$ represents the position of a marker point on the interface Γ_i and $\mathbf{U}_i$ is the velocity at $\mathbf{X}_i$. Please refer to Refs. [75,77] for more details.

3 Surface Tension Force

We describe how to define the surface tension force for LSM, PFM, and IBM.

3.1 LSM. In LSM, the surface tension force is given by

$$\mathbf{SF} = -\sigma\nabla\cdot\left(\frac{\nabla\phi}{|\nabla\phi|}\right)\delta_\alpha(\phi)\frac{\nabla\phi}{|\nabla\phi|} \tag{15}$$

Here, ϕ is the level set function, and the interface curvature $\kappa(\phi)$ can be calculated by $\kappa(\phi) = \nabla \cdot (\nabla\phi/|\nabla\phi|)$. σ is the surface tension coefficient. Using Ref. [68], the smoothed δ function $\delta_\alpha(\phi)$ [8,9] is defined as

$$\delta_\alpha(\phi) = \begin{cases} \dfrac{1}{2\alpha} + \dfrac{1}{2\alpha}\cos\left(\dfrac{\pi\phi}{\alpha}\right), & \text{if} \quad |\phi| \le \alpha, \\ 0, & \text{otherwise} \end{cases} \tag{16}$$

3.2 PFM. In PFM, a surface tension force formulation, based on CSF, is given by

$$\mathbf{SF}_1 = -\frac{3\sqrt{2}}{4}\sigma\varepsilon\nabla\cdot\left(\frac{\nabla\phi}{|\nabla\phi|}\right)|\nabla\phi|\nabla\phi \tag{17}$$

Here, ϕ is the phase-field function, and ε is a small positive parameter in Eqs. (7) and (8). $\mathbf{SF}_1$ comes from the CSF framework [54]. Similar to the surface tension formula in LSM, $\nabla \cdot (\nabla\phi/|\nabla\phi|)$ accounts for the interface curvature $\kappa(\phi)$. We note that some other surface tension force formulas driven by thermodynamics are frequently used in PFM for two-phase flows. These include:

$$\mathbf{SF}_2 = \frac{3\sqrt{2}}{4}\sigma\varepsilon\nabla\cdot\left(|\nabla\phi|^2 I - \nabla\phi\otimes\nabla\phi\right) \tag{18}$$

$$\mathbf{SF}_3 = \frac{3\sqrt{2}\sigma}{4\varepsilon}\mu\nabla\phi \tag{19}$$

$$\mathbf{SF}_4 = -\frac{3\sqrt{2}\sigma}{4\varepsilon}\phi\nabla\mu \tag{20}$$

where I is the unit tensor δ_{ij} and the term $\nabla\phi\otimes\nabla\phi$ is the usual tensor product defined by $(\nabla\phi\otimes\nabla\phi)_{ij} = (\partial\phi/\partial x_i)(\partial\phi/\partial x_j)$

In $\mathbf{SF}_2$, $\nabla\phi\otimes\nabla\phi$ is induced elastic stress due to the mixing of the different species [36,48]. $\mathbf{SF}_3$ was derived in Ref. [38]. $\mathbf{SF}_4$, chemical potential formulation, was proposed by Ref. [41]. The formulas for **SF** that have been applied in the literature are as follows: $\mathbf{SF}_1$ [54,60,61], $\mathbf{SF}_2$ [36,40,44,45,48,52,], $\mathbf{SF}_3$ [37,38,43,46], and $\mathbf{SF}_4$ [41,42,49,58,60].

3.3 IBM. In IBM, the surface tension force is given by

$$\mathbf{SF}(\mathbf{x},t) = \int_\Gamma \mathbf{f}(s,t)\delta^2(\mathbf{x} - \mathbf{X}(s,t))ds \tag{21}$$

$$\mathbf{f}(s,t) = \sigma \frac{\partial^2 \mathbf{X}(s,t)}{\partial s^2} \tag{22}$$

where $\mathbf{f}(s,t)$ is the boundary force density. Note that $\partial^2 \mathbf{X}(s,t)/\partial s^2$ accounts for the interface curvature κ.

4 Variable Density and Viscosity

The density and viscosity are constant within a fluid but can take different values in each phase. Here, the three methods use a similar tactic to identify the different phases. Let ρ_i and η_i, $i = 1$, 2, be the density and viscosity of fluid i, respectively. The density and viscosity values are determined by

$$\rho = \rho_2 + (\rho_1 - \rho_2)H \tag{23}$$

$$\eta = \eta_2 + (\eta_1 - \eta_2)H \tag{24}$$

where H is the Heaviside (step) function whose value is one in fluid 1 and zero in fluid 2. We illustrate the three discrete Heaviside functions used in the three methods in Fig. 6.

4.1 LSM. For LSM, because the jump in phase properties across the interface may lead to numerical difficulties, it needs to be smoothed [8]. Hence, $H(\phi)$ is replaced by a smoothed Heaviside function as

$$H_\alpha(\phi) = \begin{cases} 0, & \text{if} \quad \phi < -\alpha, \\ \frac{1}{2}\left[1 + \frac{\phi}{\alpha} + \frac{1}{\pi}\sin\left(\frac{\pi\phi}{\alpha}\right)\right], & \text{if} \quad |\phi| \le \alpha, \\ 1, & \text{if} \quad \phi > \alpha \end{cases} \tag{25}$$

where 2α corresponds to the interface thickness ($\alpha > 0$). Note that $H'_\alpha(\phi) = \delta_\alpha(\phi)$. The regularized density and viscosity are then defined as

$$\rho(\phi) = \rho_2 + (\rho_1 - \rho_2)H_\alpha(\phi) \tag{26}$$

$$\eta(\phi) = \eta_2 + (\eta_1 - \eta_2)H_\alpha(\phi) \tag{27}$$

The interface thickness depends on the grid size h and should be chosen as small as possible for accuracy but large enough to stabilize the system. When α is relatively small, e.g., $\alpha = 0.5h$, the interface tends to be staggered. In contrast, if α is relatively large, e.g., $\alpha = 3.0h$, the interface tends to be smeared. The values of α that have been applied in the literature are as follow: $0.5h$ [24], h [33], $1.5h$ [8,21,26], $2h$ [12,28], $2.5h$ [9], and $3h$ [12].

4.2 PFM. The density and viscosity are linear functions of the phase field [47,54]. The density and viscosity of the mixture are defined as

$$\rho(\phi) = \rho_2 + (\rho_1 - \rho_2)\frac{1+\phi}{2} \tag{28}$$

$$\eta(\phi) = \eta_2 + (\eta_1 - \eta_2)\frac{1+\phi}{2} \tag{29}$$

The harmonic interpolation for the variable density and viscosity can also be used [48] as

$$\frac{1}{\rho(\phi)} = \frac{1}{2}\left(\frac{1+\phi}{\rho_1} + \frac{1-\phi}{\rho_2}\right) \tag{30}$$

$$\frac{1}{\eta(\phi)} = \frac{1}{2}\left(\frac{1+\phi}{\eta_1} + \frac{1-\phi}{\eta_2}\right) \tag{31}$$

4.3 IBM. For IBM, we introduce an indicator function $H(\mathbf{x},t)$ [70], which has the characteristics of the Heaviside function. Let us define a gradient field

$$\nabla H(\mathbf{x},t) = -\int_\Gamma \mathbf{n}(\mathbf{X}(s,t))\delta^2(\mathbf{x} - \mathbf{X}(s,t))ds \tag{32}$$

which is nonzero near the interface and zero in the other domain. To find the indicator function, we solve Poisson's equation

$$\Delta H(\mathbf{x},t) = -\nabla \cdot \int_\Gamma \mathbf{n}(\mathbf{X}(s,t))\delta^2(\mathbf{x} - \mathbf{X}(s,t))ds \tag{33}$$

with the Dirichlet boundary condition. Then, the variable fluid properties ρ and μ can be represented by

$$\rho(H) = \rho_2 + (\rho_1 - \rho_2)H \tag{34}$$

$$\eta(H) = \eta_2 + (\eta_1 - \eta_2)H \tag{35}$$

5 Volume Conservation

5.1 LSM. One of the main drawbacks of LSM is its lack of mass conservation. This leads to nonphysical motions of the interface, which severely deteriorate the accuracy and stability of the simulation results [10]. Several methods for improving mass conservation have been proposed. The authors in Refs. [13,22,32] take full advantage of LSM for better curvature approximation using the volume of fluid (VOF) method. In Refs. [14,30], a boundary condition capturing method developed from the ghost fluid method (GFM) models the pressure jump directly, leading to no need to add the surface tension force **SF**. The surface tension is modeled directly by imposing a pressure jump across the interface. The exact jumps in density and viscosity are allowed so that the nonphysical finite width interface smeared by δ function can be replaced by a sharp interface. In Refs. [17,27], the authors presented a hybrid particle LSM to improve the mass conservation and interface resolution by using Lagrangian marker particles to rebuild the level set in underresolved regions.

Besides the above studies, in Refs. [24,31], the authors demonstrated another way to conserve mass. Instead of using a reinitialization process, they use the regularized characteristic function. An initialization step, formulated as a conservation law, is used to preserve the smooth profile. Another technique is the so-called volume-fraction level set approach [25], where an alternative formulation of the Heaviside function is used for property evaluation and mass conservation correction.

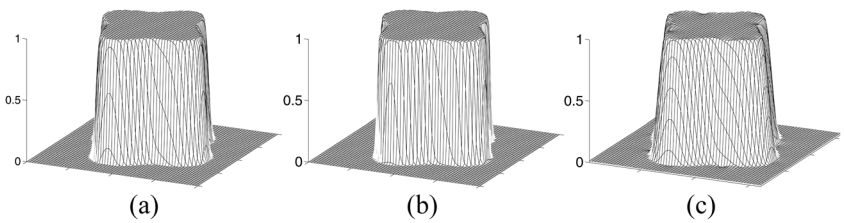

Fig. 6 (*a*) Smoothed Heaviside function $H_\alpha(\phi)$ for LSM, (*b*) $(1+\phi)/2$ for PFM, and (*c*) Indicator function *H* for IBM.

Recently, a geometry-based reinitialization scheme for the level set function was compared to the widely used partial differential equation-based scheme [34]. The authors show that the algorithm is well suited to curvilinear grids, and mass is also conserved by means of a localized mass correction.

5.2 PFM. As the evolution of the phase-field function ϕ is governed by the fourth-order Cahn–Hilliard equation, which naturally conserves mass, and because there is a critical balance between nonlinear and diffusive terms, the solution's thin transition layers do not deteriorate dynamically [57,64]. However, in Ref. [57], the authors pointed out that, even though the phase-field variable ϕ is conserved globally, simulating two-phase flows with Cahn–Hilliard diffusion causes a droplet to shrink spontaneously when ϕ shifts from its expected values in the bulk phase. In addition, the global mass conservation does not imply that the mass enclosed by the zero contour of ϕ remains constant.

We note that there is another approach in PFM using the Allen–Cahn equation [56,62,65]. Its implementation is easier than using the Cahn–Hilliard equation because only second-order derivative term is shown in the Allen–Cahn equation.

5.3 IBM. When an exact projection method is used to solve the Navier–Stokes equations, the velocity field on the Eulerian grid is discretely divergence-free. However, this does not guarantee that the velocity field interpolated by the δ function is continuously divergence-free. This results in a loss of volume for a closed interface [71,85]. Furthermore, because the interface moves in a discrete manner, there is also a lack of volume conservation in this process. In Refs. [90,91], the authors developed a volume-preserving scheme with negligibly additional computational cost. This scheme corrects the interface location normal to the interface so that the volume of one fluid remains constant.

When high Reynolds numbers are used, the local accuracy of the interface is important, and the smooth force distribution is less desirable. Thus, many researchers have considered that the sharp interface is represented by using the immersed boundary, including the immersed interface methods (IIM) [93–96]. The force term is heavily connected with the employed discretization schemes. Besides solving two-phase flows, there are many studies for simulating flows in the complex boundaries; refer to Refs. [97–101].

6 Numerical Solution

In this section, we present a series of numerical solutions on a staggered marker-and-cell mesh [102] in which pressure and indicator functions are stored at the cell centers and velocities are defined at the cell edges (Fig. 7(*a*)). Let a computational domain $\Omega = (a,b) \times (c,d)$ be partitioned in Cartesian geometry. Let N_x and N_y be the number of cells in the x- and y-directions, respectively. We assume a uniform mesh with mesh spacing $h = (b-a)/N_x = (d-c)/N_y$. The center of each cell Ω_{ij} is located at $\mathbf{x}_{ij} = (x_i, y_j) = (a + (i-0.5)h, c + (j-0.5)h)$ for $i = 1, \ldots, N_x$ and $j = 1, \ldots, N_y$. We denote the discrete computational domain $\Omega_h = \{\mathbf{x}_{ij}\}$. In IBM, N Lagrangian points $\mathbf{X}_l^n = (x_l^n, y_l^n)$ for $l = 1, \ldots, N$ are used to discretize the immersed boundary (Fig. 7(*b*)). In LSM and PFM, a grid function ϕ_{ij} is used.

At the n-th time step, we have a velocity field $\mathbf{u}^n$, which is divergence-free, and a surface tension calculated by ϕ^n (or the boundary configuration $\mathbf{X}^n$). We seek $\mathbf{u}^{n+1}$, p^{n+1}, and ϕ^{n+1} (or $\mathbf{X}^{n+1}$) that are the solutions of the following semi-implicit scheme:

$$\rho^n \frac{\mathbf{u}^{n+1} - \mathbf{u}^n}{\Delta t} = -\rho^n \mathbf{u}^n \cdot \nabla_d \mathbf{u}^n - \nabla_d p^{n+1} + \nabla_d \cdot \left[\eta^n \left(\nabla_d \mathbf{u}^n + (\nabla_d \mathbf{u}^n)^T \right) \right] + \mathbf{SF}^n + \rho^n \mathbf{g} \tag{36}$$

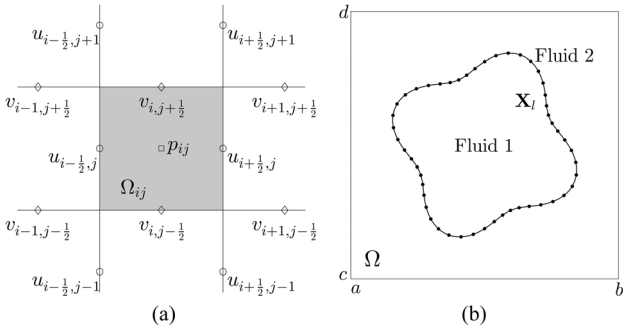

Fig. 7 (*a*) Velocities and pressure near the cell Ω_{ij} and (*b*) Lagrangian points $\mathbf{X}_l$ in the computational domain Ω.

$$\nabla_d \cdot \mathbf{u}^{n+1} = 0 \tag{37}$$

where $\mathbf{g} = (0, -g)$, with g being the gravitational acceleration. Here, $\nabla_d \cdot$ and ∇_d are the discrete divergence and gradient operators, respectively. The projection method, introduced by Chorin [103], is applied to solve the incompressible Navier–Stokes equations. We refer the readers to Refs. [8,12,90,91,102] for the discretization approach. An outline of the main procedures in one time step is as follows:

Step 1. Compute the surface tension force $\mathbf{SF}^n$ using ϕ^n (or $\mathbf{X}^n$). A detailed description of the discretization of $\mathbf{SF}^n$ for each method is given in Sec. 6.1. We calculate the density ρ^n and viscosity η^n using ϕ^n (or $\mathbf{X}^n$). The numerical formulas for the variable density and viscosity are drawn in Sec. 6.2.

Step 2. Solve the Navier–Stokes equations to get $\mathbf{u}^{n+1}$ and p^{n+1} from $\mathbf{u}^n$ and $\mathbf{SF}^n$. We first solve an intermediate velocity field $\tilde{\mathbf{u}}^n$:

$$\frac{\tilde{\mathbf{u}}^n - \mathbf{u}^n}{\Delta t} + \mathbf{u}^n \cdot \nabla_d \mathbf{u}^n = \frac{1}{\rho^n} \nabla_d \cdot \left[\eta^n \left(\nabla_d \mathbf{u}^n + (\nabla_d \mathbf{u}^n)^T \right) \right] + \frac{1}{\rho^n} \mathbf{SF}^n + \mathbf{g} \tag{38}$$

The resulting finite difference equations are written out explicitly:

$$\tilde{u}^n_{i+\frac{1}{2},j} = u^n_{i+\frac{1}{2},j} - \Delta t (u u_x + v u_y)^n_{i+\frac{1}{2},j} + \frac{\Delta t}{\rho^n_{i+\frac{1}{2}j}} SF^{x-\text{edge}}_{i+\frac{1}{2},j} + \frac{\Delta t}{\rho^n_{i+\frac{1}{2},j}} \left(2(\eta u_x)_x + (\eta u_y)_y + (\eta v_x)_y \right)^n_{i+\frac{1}{2},j} \tag{39}$$

$$\tilde{v}^n_{i,j+\frac{1}{2}} = v^n_{i,j+\frac{1}{2}} - \Delta t (u v_x + v v_y)^n_{i,j+\frac{1}{2}} + \frac{\Delta t}{\rho^n_{i,j+\frac{1}{2}}} SF^{y-\text{edge}}_{i,j+\frac{1}{2}} + \frac{\Delta t}{\rho^n_{i,j+\frac{1}{2}}} \left((\eta v_x)_x + (\eta u_y)_x + 2(\eta v_y)_y \right)^n_{i,j+\frac{1}{2}} - g\Delta t \tag{40}$$

where we define $\rho^n_{i+\frac{1}{2},j} = \left(\rho^n_{i+1,j} + \rho^n_{ij}\right)/2$. $\rho^n_{i,j+\frac{1}{2}}$, $SF^{x-\text{edge}}_{i+\frac{1}{2},j}$, and $SF^{y-\text{edge}}_{i,j+\frac{1}{2}}$ are similarly defined. The advection terms are defined by

$$(u u_x + v u_y)^n_{i+\frac{1}{2},j} = u^n_{i+\frac{1}{2},j} \bar{u}^n_{x_{i+\frac{1}{2},j}} + \frac{1}{4} \left(v^n_{i,j-\frac{1}{2}} + v^n_{i+1,j-\frac{1}{2}} + v^n_{i,j+\frac{1}{2}} + v^n_{i+1,j+\frac{1}{2}} \right) \bar{u}^n_{y_{i+\frac{1}{2},j}} \tag{41}$$

and

$$(u v_x + v v_y)^n_{i,j+\frac{1}{2}} = v^n_{i,j+\frac{1}{2}} \bar{v}^n_{y_{i,j+\frac{1}{2}}} + \frac{1}{4} \left(u^n_{i-\frac{1}{2},j} + u^n_{i-\frac{1}{2},j+1} + u^n_{i+\frac{1}{2},j} + u^n_{i+\frac{1}{2},j+1} \right) \bar{v}^n_{x_{i,j+\frac{1}{2}}} \tag{42}$$

where the values $\bar{u}^n_{x_{i+\frac{1}{2},j}}$ and $\bar{u}^n_{y_{i+\frac{1}{2},j}}$ are computed using the upwind procedure

$$\bar{u}^n_{x_{i+\frac{1}{2},j}} = \begin{cases} \dfrac{u^n_{i+\frac{1}{2},j} - u^n_{i-\frac{1}{2},j}}{h}, & \text{if} \quad u^n_{i+\frac{1}{2},j} > 0, \\ \dfrac{u^n_{i+\frac{3}{2},j} - u^n_{i+\frac{1}{2},j}}{h}, & \text{otherwise} \end{cases} \tag{43}$$

and

$$\bar{u}^n_{y_{i+\frac{1}{2},j}} = \begin{cases} \dfrac{u^n_{i+\frac{1}{2},j} - u^n_{i+\frac{1}{2},j-1}}{h}, & \text{if } v^n_{i,j-\frac{1}{2}} + v^n_{i+1,j-\frac{1}{2}} + v^n_{i,j+\frac{1}{2}} + v^n_{i+1,j+\frac{1}{2}} > 0, \\ \dfrac{u^n_{i+\frac{1}{2},j+1} - u^n_{i+\frac{1}{2},j}}{h}, & \text{otherwise} \end{cases} \tag{44}$$

The quantities $\bar{v}^n_{x_{i,j+\frac{1}{2}}}$ and $\bar{v}^n_{y_{i,j+\frac{1}{2}}}$ are similarly computed. The viscosity terms are defined by

$$\begin{aligned} \left(2(\eta u_x)_x + (\eta u_y)_y + (\eta v_x)_y\right)^n_{i+\frac{1}{2},j} = {} & \frac{2}{h}\left(\eta^n_{i+1,j}\frac{u^n_{i+\frac{3}{2},j} - u^n_{i+\frac{1}{2},j}}{h} - \eta^n_{ij}\frac{u^n_{i+\frac{1}{2},j} - u^n_{i-\frac{1}{2},j}}{h}\right) + \frac{1}{4}\left(\eta^n_{i+1,j+1} + \eta^n_{i,j+1} + \eta^n_{ij} + \eta^n_{i+1,j}\right)\frac{u^n_{i+\frac{1}{2},j+1} - u^n_{i+\frac{1}{2},j}}{h^2} \\ & - \frac{1}{4}\left(\eta^n_{i+1,j} + \eta^n_{ij} + \eta^n_{i,j-1} + \eta^n_{i+1,j-1}\right)\frac{u^n_{i+\frac{1}{2},j} - u^n_{i+\frac{1}{2},j-1}}{h^2} + \frac{1}{4}\left(\eta^n_{i+1,j+1} + \eta^n_{i,j+1} + \eta^n_{ij} + \eta^n_{i+1,j}\right) \\ & \times \frac{v^n_{i+1,j+\frac{1}{2}} - v^n_{i,j+\frac{1}{2}}}{h^2} - \frac{1}{4}\left(\eta^n_{i+1,j} + \eta^n_{ij} + \eta^n_{i,j-1} + \eta^n_{i+1,j-1}\right)\frac{v^n_{i,j-\frac{1}{2}} - v^n_{i-1,j-\frac{1}{2}}}{h^2} \end{aligned} \tag{45}$$

and

$$\begin{aligned} \left((\eta v_x)_x + (\eta u_y)_x + 2(\eta v_y)_y\right)^n_{i,j+\frac{1}{2}} = {} & \frac{1}{4}\left(\eta^n_{i+1,j+1} + \eta^n_{i,j+1} + \eta^n_{ij} + \eta^n_{i+1,j}\right)\frac{v^n_{i+1,j+\frac{1}{2}} - v^n_{i,j+\frac{1}{2}}}{h^2} - \frac{1}{4}\left(\eta^n_{i+1,j} + \eta^n_{ij} + \eta^n_{i,j-1} + \eta^n_{i+1,j-1}\right) \\ & \times \frac{v^n_{i,j+\frac{1}{2}} - v^n_{i-1,j+\frac{1}{2}}}{h^2} + \frac{1}{4}\left(\eta^n_{i+1,j+1} + \eta^n_{i,j+1} + \eta^n_{ij} + \eta^n_{i+1,j}\right)\frac{u^n_{i+\frac{1}{2},j+1} - u^n_{i+\frac{1}{2},j}}{h^2} \\ & - \frac{1}{4}\left(\eta^n_{i+1,j} + \eta^n_{ij} + \eta^n_{i,j-1} + \eta^n_{i+1,j-1}\right)\frac{u^n_{i+\frac{1}{2},j} - u^n_{i+\frac{1}{2},j-1}}{h^2} \\ & + \frac{2}{h}\left(\eta^n_{i,j+1}\frac{v^n_{i,j+\frac{3}{2}} - v^n_{i,j+\frac{1}{2}}}{h} - \eta^n_{ij}\frac{v^n_{i,j+\frac{1}{2}} - v^n_{i,j-\frac{1}{2}}}{h}\right) \end{aligned} \tag{46}$$

We then solve the following equations for the advanced pressure field at the $(n+1)$-th time step:

$$\frac{\mathbf{u}^{n+1} - \tilde{\mathbf{u}}^n}{\Delta t} = -\frac{1}{\rho^n}\nabla_d p^{n+1} \tag{47}$$

$$\nabla_d \cdot \mathbf{u}^{n+1} = 0 \tag{48}$$

Applying the discrete divergence operator and divergence-free Eq. (48) to Eq. (47), we obtain Poisson's equation for the pressure at the time $(n+1)$:

$$\nabla_d \cdot \left(\frac{1}{\rho^n}\nabla_d p^{n+1}\right) = \frac{1}{\Delta t}\nabla_d \cdot \tilde{\mathbf{u}}^n \tag{49}$$

where

$$\begin{aligned} \nabla_d \cdot \left(\frac{1}{\rho^n}\nabla_d p^{n+1}\right)_{ij} = {} & \frac{p^{n+1}_{i+1,j} - p^{n+1}_{ij}}{h^2\rho^n_{i+\frac{1}{2},j}} - \frac{p^{n+1}_{ij} - p^{n+1}_{i-1,j}}{h^2\rho^n_{i-\frac{1}{2},j}} \\ & + \frac{p^{n+1}_{i,j+1} - p^{n+1}_{ij}}{h^2\rho^n_{i,j+\frac{1}{2}}} - \frac{p^{n+1}_{ij} - p^{n+1}_{i,j-1}}{h^2\rho^n_{i,j-\frac{1}{2}}} \end{aligned} \tag{50}$$

and

$$\nabla_d \cdot \tilde{\mathbf{u}}^n_{ij} = \frac{\tilde{u}^n_{i+\frac{1}{2},j} - \tilde{u}^n_{i-\frac{1}{2},j}}{h} + \frac{\tilde{v}^n_{i,j+\frac{1}{2}} - \tilde{v}^n_{i,j-\frac{1}{2}}}{h} \tag{51}$$

The boundary condition for the pressure is

$$\begin{aligned} \mathbf{n} \cdot \nabla_d p^{n+1} = \mathbf{n} \cdot \Bigg(& -\rho^n\frac{\mathbf{u}^{n+1} - \mathbf{u}^n}{\Delta t} - \rho^n(\mathbf{u} \cdot \nabla_d \mathbf{u})^n \\ & + \left[\eta^n\left(\nabla_d \mathbf{u}^n + (\nabla_d \mathbf{u}^n)^T\right)\right] + \mathbf{SF}^n + \rho^n \mathbf{g}\Bigg) \end{aligned} \tag{52}$$

where $\mathbf{n}$ is the unit normal vector to the domain boundary. For example, if we use a periodic boundary condition on the horizontal boundaries and Dirichlet condition on the top and bottom boundaries, then Eq. (52) is reduced as

$$\mathbf{n} \cdot \nabla_d p^{n+1} = \mathbf{n} \cdot (\mathbf{SF}^n + \rho^n \mathbf{g}) \tag{53}$$

The resulting linear system of Eq. (49) is solved using a multigrid method [104], specifically V-cycles with a Gauss–Seidel relaxation. The divergence-free velocities u^{n+1} and v^{n+1} are then obtained using Eq. (47):

$$u_{i+\frac{1}{2},j}^{n+1} = \tilde{u}_{i+\frac{1}{2},j}^{n} - \frac{\Delta t}{\rho_{i+\frac{1}{2},j}^{n} h}\left(p_{i+1,j}^{n+1} - p_{ij}^{n+1}\right) \tag{54}$$

$$v_{i,j+\frac{1}{2}}^{n+1} = \tilde{v}_{i,j+\frac{1}{2}}^{n} - \frac{\Delta t}{\rho_{i,j+\frac{1}{2}}^{n} h}\left(p_{i,j+1}^{n+1} - p_{ij}^{n+1}\right) \tag{55}$$

Step 3. Once the updated fluid velocity $\mathbf{u}^{n+1}$ has been determined, we can find the new level set and phase-field ϕ^{n+1} (or $\mathbf{X}^{n+1}$). We will describe this in Sec. 6.3.

This completes a single time step.

6.1 Discretization of Surface Tension Force. In this section, we present the discretization of the surface tension forces.

6.1.1 LSM. In LSM, the surface tension force is given by

$$\mathbf{SF}_{ij}^{n} = -\sigma \nabla_d \cdot \left(\frac{\mathbf{m}}{|\mathbf{m}|}\right)_{ij} \delta_\alpha(\phi_{ij}) \frac{\nabla_d \phi_{ij}}{|\nabla_d \phi_{ij}|} \tag{56}$$

Vertex-centered normal vectors are obtained by differentiating the level set in the four surrounding cells. For example, the normal vector at the top right vertex of cell Ω_{ij} is given by

$$\begin{aligned}
&\mathbf{m}_{i+\frac{1}{2},j+\frac{1}{2}} \\
&= \left(m_{i+\frac{1}{2},j+\frac{1}{2}}^{x}, m_{i+\frac{1}{2},j+\frac{1}{2}}^{y}\right) \\
&= \left(\frac{\phi_{i+1,j} + \phi_{i+1,j+1} - \phi_{ij} - \phi_{i,j+1}}{2h}, \frac{\phi_{i,j+1} + \phi_{i+1,j+1} - \phi_{ij} - \phi_{i+1,j}}{2h}\right)
\end{aligned} \tag{57}$$

The curvature is calculated at cell centers from the vertex-centered normals [5] and is given by

$$\begin{aligned}
\kappa(\phi_{ij}) &= \nabla_d \cdot \left(\frac{\mathbf{m}}{|\mathbf{m}|}\right)_{ij} \\
&= \frac{1}{2h}\left(\frac{m_{i+\frac{1}{2},j+\frac{1}{2}}^{x} + m_{i+\frac{1}{2},j+\frac{1}{2}}^{y}}{|\mathbf{m}_{i+\frac{1}{2},j+\frac{1}{2}}|} + \frac{m_{i+\frac{1}{2},j-\frac{1}{2}}^{x} - m_{i+\frac{1}{2},j-\frac{1}{2}}^{y}}{|\mathbf{m}_{i+\frac{1}{2},j-\frac{1}{2}}|}\right. \\
&\quad \left. - \frac{m_{i-\frac{1}{2},j+\frac{1}{2}}^{x} - m_{i-\frac{1}{2},j+\frac{1}{2}}^{y}}{|\mathbf{m}_{i-\frac{1}{2},j+\frac{1}{2}}|} - \frac{m_{i-\frac{1}{2},j-\frac{1}{2}}^{x} + m_{i-\frac{1}{2},j-\frac{1}{2}}^{y}}{|\mathbf{m}_{i-\frac{1}{2},j-\frac{1}{2}}|}\right)
\end{aligned} \tag{58}$$

The cell-centered normal is the average of the vertex normals:

$$\nabla_d \phi_{ij} = \frac{\mathbf{m}_{i+\frac{1}{2},j+\frac{1}{2}} + \mathbf{m}_{i+\frac{1}{2},j-\frac{1}{2}} + \mathbf{m}_{i-\frac{1}{2},j+\frac{1}{2}} + \mathbf{m}_{i-\frac{1}{2},j-\frac{1}{2}}}{4} \tag{59}$$

6.1.2 PFM. In PFM, the surface tension force is given by

$$\mathbf{SF}_{ij}^{n} = -\frac{3\sqrt{2}}{4}\sigma\varepsilon\nabla_d \cdot \left(\frac{\mathbf{m}}{|\mathbf{m}|}\right)_{ij} |\nabla_d \phi_{ij}| \nabla_d \phi_{ij} \tag{60}$$

where the discretization is similar to that in LSM.

Figure 8 shows examples of the smoothed δ function $\delta_\alpha(\phi)$ and $\varepsilon|\nabla\phi|^2$ for LSM and PFM, respectively. The level set $\phi = x$ and phase-field $\phi = \tanh(x/(\sqrt{2}\varepsilon))$ functions are given for each method. The other parameters $h = 1/32$, $\alpha = 3h$, and $\varepsilon = 6h/[2\sqrt{2}\tanh^{-1}(0.9)]$ are used.

6.1.3 IBM. In IBM, the discretization of the force density $\mathbf{f}^n$ is defined by the boundary configuration $\mathbf{X}^n$. For $l = 1, \ldots, N$,

$$\mathbf{f}_l^n = \frac{\sigma}{\Delta s_{l+\frac{1}{2}}}\left(\frac{\mathbf{X}_{l+1}^n - \mathbf{X}_l^n}{\Delta s_{l+1}} - \frac{\mathbf{X}_l^n - \mathbf{X}_{l-1}^n}{\Delta s_l}\right) \tag{61}$$

where $\Delta s_l = \sqrt{(x_l - x_{l-1})^2 + (y_l - y_{l-1})^2}$ is the Lagrangian mesh size and σ is a surface tension coefficient. Here, $\Delta s_{l+\frac{1}{2}} = (\Delta s_l + \Delta s_{l+1})/2$. For implementation, because the interface is close, $\mathbf{X}_0^n = \mathbf{X}_N^n$ and $\mathbf{X}_{N+1}^n = \mathbf{X}_1^n$. The boundary force is then spread into the nearby lattice points of the fluid:

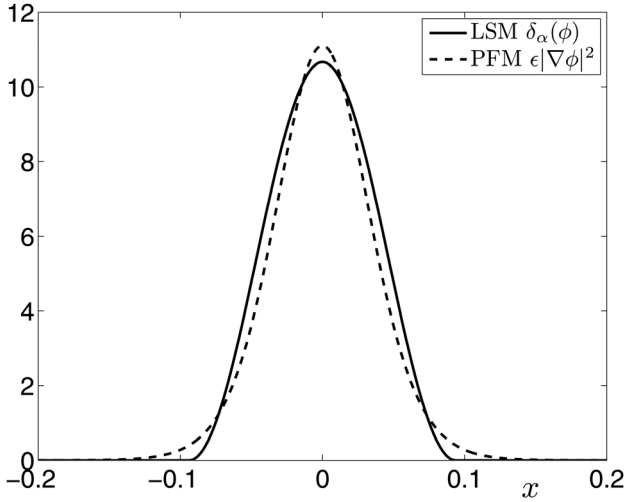

Fig. 8 Smoothed δ functions for LSM and PFM with $h = 1/32$, $\alpha = 3h$, and $\varepsilon = 6h/[2\sqrt{2}\tanh^{-1}(0.9)]$

$$\mathbf{SF}_{ij}^{n} = \sum_{l=1}^{N} \mathbf{f}_l^n \delta_h^2(\mathbf{x}_{ij} - \mathbf{X}_l^n)\Delta s_{l+\frac{1}{2}} \tag{62}$$

for $i = 1, \ldots, N_x$ and $j = 1, \ldots, N_y$, where δ_h^2 is a two-dimensional discrete δ function:

$$\delta_h^2(\mathbf{x}) = \frac{1}{h^2}\psi\left(\frac{x}{h}\right)\psi\left(\frac{y}{h}\right) \tag{63}$$

where $\psi(r)/h$ is a one-dimensional discrete δ function. Common δ functions include two-point, three-point, four-point, six-point, and four-point cosine functions [78,83,86]. The motivation for this particular choice of the function $\psi(r)$ is given in Refs. [68,78]. The formulas that have been applied in the literature are as follows: two-point [93], three-point [76,87], four-point [90,91], six-point [73,84], and four-point cosine [68,71,80,89]. $\psi(r)$ for the δ functions are as follows:

two-point function

$$\psi(r) = \begin{cases} 1 - |r|, & \text{if} \quad |r| \le 1, \\ 0, & \text{otherwise} \end{cases} \tag{64}$$

three-point function

$$\psi(r) = \begin{cases} \dfrac{1 + \sqrt{-3r^2 + 1}}{3}, & \text{if} \quad |r| \le \dfrac{1}{2}, \\ \dfrac{5 - 3|r| - \sqrt{-3(1 - |r|)^2 + 1}}{6}, & \text{if} \quad \dfrac{1}{2} \le |r| \le \dfrac{3}{2}, \\ 0, & \text{otherwise} \end{cases} \tag{65}$$

four-point function

$$\psi(r) = \begin{cases} \dfrac{3 - 2|r| + \sqrt{1 + 4|r| - 4r^2}}{8}, & \text{if} \quad |r| \le 1, \\ \dfrac{5 - 2|r| - \sqrt{-7 + 12|r| - 4r^2}}{8}, & \text{if} \quad 1 \le |r| \le 2, \\ 0, & \text{otherwise} \end{cases} \tag{66}$$

six-point function

$$\psi(r)=\begin{cases}\dfrac{61}{112}-\dfrac{11}{42}|r|-\dfrac{11}{56}r^2+\dfrac{1}{12}|r|^3+\dfrac{\sqrt{3}}{336}(243+1584|r|-748r^2 & \\ -1560|r|^3+500r^4+336|r|^5-112r^6)^{1/2}, & \text{if} \quad 0\le|r|\le 1,\\ \dfrac{21}{16}+\dfrac{7}{12}|r|-\dfrac{7}{8}r^2+\dfrac{1}{6}|r|^3-\dfrac{3}{2}\psi(|r|-1), & \text{if} \quad 1\le|r|\le 2,\\ \dfrac{9}{8}-\dfrac{23}{12}|r|+\dfrac{3}{4}r^2-\dfrac{1}{12}|r|^3+\frac{1}{2}\psi(|r|-2), & \text{if} \quad 2\le|r|\le 3,\\ 0, & \text{otherwise}\end{cases} \tag{67}$$

four-point cosine function

$$\psi(r)=\begin{cases}\dfrac{1+\cos(\pi r/2)}{4}, & \text{if} \quad |r|\le 2,\\ 0, & \text{otherwise}\end{cases} \tag{68}$$

The discrete δ functions may produce nonphysical force oscillations when dealing with moving boundaries or free interfaces. However, the oscillations can be controlled by careful selection of the discrete δ function [82]. In Ref. [86], the authors carried out the stability analysis of the feedback forcing scheme for the virtual boundary method for various types of regularized δ functions. They showed that the stability regime could be widen by including more supported points for the δ function. A smoothing technique was developed to construct the discrete functions from regular ones, which can significantly reduce the nonphysical oscillations [88]. For example, a smoothed four-point function ψ^* can be written as

$$\psi^*(r)=\begin{cases}\dfrac{12+\pi-8r^2}{32}, & \text{if} \quad 0\le|r|\le\frac{1}{2},\\ \dfrac{2+(1-|r|)\sqrt{-2+8|r|-4r^2}}{8}-\dfrac{\arcsin\left(\sqrt{2}(|r|-1)\right)}{8}, & \text{if} \quad \dfrac{1}{2}\le|r|\le\dfrac{3}{2},\\ \dfrac{68-\pi-48|r|+8r^2}{64}+\dfrac{(|r|-2)\sqrt{-14+16|r|-4r^2}}{16}+\dfrac{\arcsin\left(\sqrt{2}(|r|-2)\right)}{16}, & \text{if} \quad \dfrac{3}{2}\le|r|\le\dfrac{5}{2},\\ 0, & \text{otherwise}\end{cases} \tag{69}$$

Figure 9(*a*) shows the regularized δ functions associated with Eqs. (64)–(67) and Fig. 9(*b*) depicts the four-point δ functions associated with four-point, four-point cosine, and smoothed four-point functions.

6.2 Variable Density and Viscosity. In this section, we present the approximations for the variable density and viscosity.

6.2.1 LSM. In LSM, we define the variable density and viscosity by

$$\rho_{ij}^n=\rho_2+(\rho_1-\rho_2)H_\alpha(\phi_{ij}^n) \tag{70}$$

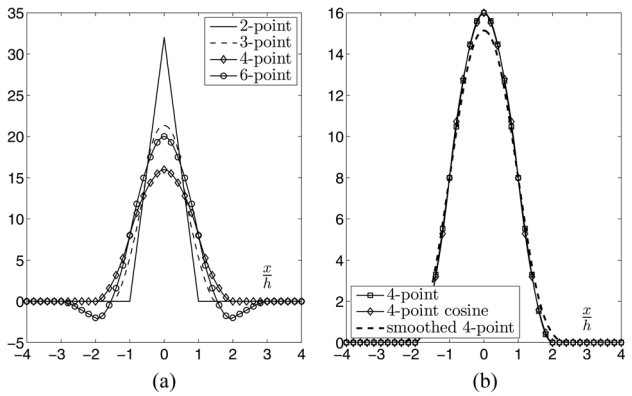

(a) (b)

Fig. 9 (*a*) Regularized delta functions and (*b*) Four-point δ functions.

$$\eta_{ij}^n=\eta_2+(\eta_1-\eta_2)H_\alpha(\phi_{ij}^n) \tag{71}$$

where $H_\alpha(\phi)$ is from Eq. (25).

6.2.2 PFM. In PFM, we define the variable density and viscosity by

$$\rho_{ij}^n=\rho_2+(\rho_1-\rho_2)\frac{1+\phi_{ij}^n}{2} \tag{72}$$

$$\eta_{ij}^n=\eta_2+(\eta_1-\eta_2)\frac{1+\phi_{ij}^n}{2} \tag{73}$$

6.2.3 IBM. We present an algorithm for the discrete indicator function [74,79,90]. Let G_{ij}^n be the discretization of the right-hand side of Eq. (32):

$$G_{ij}^n=\sum_{i=1}^{N}\mathbf{n}_l^n\delta_h^2(\mathbf{x}_{ij}-\mathbf{X}_l^n)\Delta s_{l+\frac{1}{2}} \tag{74}$$

where $\Delta s_{l+\frac{1}{2}}=(\Delta s_1+\Delta s_{l+1})/2$. To calculate the unit normal vector $\mathbf{n}_l^n$ at $\mathbf{X}_l^n$, we use a quadratic polynomial approximation with three points $\mathbf{X}_{l-1}^n$, $\mathbf{X}_l^n$, and $\mathbf{X}_{l+1}^n$. First, let $x(s)=\alpha_1 s^2+\beta_1 s+\gamma_1$ and $y(s)=\alpha_2 s^2+\beta_2 s+\gamma_2$, and assume $(x(-\Delta s_l),y(-\Delta s_l))=\mathbf{X}_{l-1}^n$, $(x(0),y(0))=\mathbf{X}_l^n$, and $(x(\Delta s_{l+1}),y(\Delta s_{l+1}))=\mathbf{X}_{l+1}^n$. We then calculate the coefficients α_1, β_1, and γ_1 as follows:

$$\begin{pmatrix}\alpha_1\\ \beta_1\\ \gamma_1\end{pmatrix}=\begin{pmatrix}\Delta s_l^2 & -\Delta s_l & 1\\ 0 & 0 & 1\\ \Delta s_{l+1}^2 & \Delta s_{l+1} & 1\end{pmatrix}^{-1}\begin{pmatrix}x(\Delta s_l)\\ x(0)\\ x(\Delta s_{l+1})\end{pmatrix} \tag{75}$$

And the coefficients α_2, β_2, and γ_2 are similarly calculated. Finally, the unit normal vector is approximated by

$$\mathbf{n}_l=\left.\frac{(y_s,-x_s)}{|(x_s,y_s)|}\right|_{s=0}=\frac{1}{\sqrt{\beta_1^2+\beta_2^2}}(\beta_2,-\beta_1) \tag{76}$$

We then solve Poisson's equation using the multigrid method [104] with homogeneous Dirichlet boundary conditions:

$$\Delta_d H_{ij}^n=\nabla_d\cdot G_{ij}^n \tag{77}$$

In IBM, we can define the variable density and viscosity by

$$\rho_{ij}^n=\rho_2+(\rho_1-\rho_2)H_{ij}^n \tag{78}$$

$$\eta_{ij}^n=\eta_2+(\eta_1-\eta_2)H_{ij}^n \tag{79}$$

6.3 Update the Interface. In this section, we describe the discretization of the interface advection process.

6.3.1 LSM. The evolution of level set ϕ is given by

$$\phi^{n+1}=\phi^n-\Delta t(\mathbf{u}^{n+1}\cdot\nabla\phi^n) \tag{80}$$

The convective term is discretized as

$$\begin{aligned}\left(\mathbf{u}^{n+1}\cdot\nabla\phi^n\right)_{ij}=&\frac{u_{i+\frac{1}{2},j}^{n+1}+u_{i-\frac{1}{2},j}^{n+1}}{2h}\left(\bar{\phi}_{i+\frac{1}{2},j}^n-\bar{\phi}_{i-\frac{1}{2},j}^n\right)\\&+\frac{v_{i,j+\frac{1}{2}}^{n+1}+v_{i,j-\frac{1}{2}}^{n+1}}{2h}\left(\bar{\phi}_{i,j+\frac{1}{2}}^n-\bar{\phi}_{i,j-\frac{1}{2}}^n\right)\end{aligned} \tag{81}$$

where the edge values $\bar{\phi}_{i\pm\frac{1}{2},j}^n$ and $\bar{\phi}_{i,j\pm\frac{1}{2}}^n$ are computed using the essentially nonoscillatory (ENO) scheme derived in Ref. [7]. For example, the procedure for computing the quantity $\bar{\phi}_{i+\frac{1}{2},j}^n$ is as follows:

$$k=\begin{cases}i, & \text{if}\quad u_{i+\frac{1}{2},j}^{n+1}\geq 0,\\ i+1, & \text{otherwise}\end{cases} \tag{82}$$

$$a=\frac{\phi_{kj}^n-\phi_{k-1,j}^n}{h} \tag{83}$$

$$b=\frac{\phi_{k+1,j}^n-\phi_{kj}^n}{h} \tag{84}$$

$$d=\begin{cases}a, & \text{if}\quad |a|\leq|b|,\\ b, & \text{otherwise}\end{cases} \tag{85}$$

$$\bar{\phi}_{i+\frac{1}{2},j}^n=\phi_{ij}^n+\frac{h}{2}d(1-2(k-i)) \tag{86}$$

The quantities $\bar{\phi}_{i,j-\frac{1}{2}}^n$ and $\bar{\phi}_{i,j\pm\frac{1}{2}}^n$ are computed in a similar manner.

6.3.2 PFM. The phase-field function ϕ^n is evolved by applying the nonlinear splitting stabilized (NLSS) scheme [105,106] to the Cahn–Hilliard equation:

$$\frac{\phi^{n+1}-\phi^n}{\Delta t}=-\nabla_d\cdot(\phi^n\mathbf{u}^{n+1})+M\Delta_d\mu^{n+1}-M\Delta_d\phi^n \tag{87}$$

$$\mu^{n+1}=(\phi^{n+1})^3-\varepsilon^2\Delta_d\phi^{n+1} \tag{88}$$

where

$$\begin{aligned}\nabla_d\cdot(\phi^n\mathbf{u}^{n+1})_{ij}=&\frac{1}{2h}\left(\left(\phi_{i+1,j}^n+\phi_{ij}^n\right)u_{i+\frac{1}{2},j}^{n+1}-\left(\phi_{ij}^n+\phi_{i-1,j}^n\right)u_{i-\frac{1}{2},j}^{n+1}\right)\\&+\frac{1}{2h}\left(\left(\phi_{i,j+1}^n+\phi_{ij}^n\right)v_{i,j+\frac{1}{2}}^{n+1}-\left(\phi_{ij}^n+\phi_{i,j-1}^n\right)v_{i,j-\frac{1}{2}}^{n+1}\right)\end{aligned} \tag{89}$$

and

$$\Delta_d\phi_{ij}^n=\frac{\phi_{i+1,j}^n+\phi_{i,j+1}^n-4\phi_{ij}^n+\phi_{i-1,j}^n+\phi_{i,j-1}^n}{h^2} \tag{90}$$

We use a nonlinear full approximation storage (FAS) multigrid method [49]. The nonlinearity is treated using one step of Newton's iteration. A pointwise Gauss–Seidel relaxation scheme is used as the smoother in the multigrid method [104].

6.3.3 IBM. Once the updated fluid velocity $\mathbf{u}^{n+1}$ has been determined, we can find the velocity $\mathbf{U}^{n+1}$ and then the new position $\mathbf{X}^{n+1}$ of the immersed boundary points. This is done using a discretization of Eqs. (9) and (10). That is, for $l=1,\ldots,N$,

$$\mathbf{U}_l^{n+1}=\sum_{i=1}^{N_x}\sum_{j=1}^{N_y}\mathbf{u}_{ij}^{n+1}\delta_h^2(\mathbf{x}_{ij}-\mathbf{X}_l^n)h^2 \tag{91}$$

$$\mathbf{X}_l^{n+1}=\mathbf{X}_l^n+\Delta t\mathbf{U}_l^{n+1} \tag{92}$$

7 Numerical Examples

In this section, we perform the following numerical examples, calculating the pressure difference, comparing the droplet deformation under shear flow, and simulating the falling droplet using each method. Throughout the experiments, we use the surface tension formula [17] for PFM and four-point function [66] for IBM. We take five reinitialization steps for LSM. The results show that five iterations are enough to accurately recover the distance function.

7.1 Pressure Difference. We theoretically and numerically calculate the pressure difference of a droplet. In the absence of viscous, gravitational, and other external forces, the pressure gradient is balanced by the surface tension force $\nabla p=\mathbf{SF}$. By Laplace's formula for an infinite cylinder surrounded by a background fluid at zero pressure, the exact pressure difference is $[p]_e=\sigma/r$, where r is the droplet radius and σ is a surface tension coefficient [5]. The numerical pressure difference $[p]_h$ is calculated by

$$[p]_h=\max_{\mathbf{x}_{ij}\in\Omega_h}p_{ij}-\min_{\mathbf{x}_{ij}\in\Omega_h}p_{ij} \tag{93}$$

where p_{ij} is the pressure in the computational domain Ω_h.

For the numerical simulation, the droplet is placed at the center of the unit domain $\Omega=(0,1)\times(0,1)$ and its radius is $r=0.25$. The pressure differences are computed with $h=1/2^n$, for $n=5$, 6, and 7. We employ $\sigma=5$ with the constant density and viscosity $\rho=1$ and $\eta=1$. Therefore, the pressure difference is $[p]_e=20$. For example, using the 64×64 mesh grid, numerical results for the pressure are shown in Fig. 10. For other parameters, we set $\alpha=0.03$ in LSM, $\varepsilon=0.03$ in PFM, and $N=800$ in IBM.

Table 1 lists the numerical pressure difference $[p]_h$ with a different mesh grid for each method. The numerical pressure difference $[p]_h$ reaches a qualitative agreement with the theoretical value as the mesh is refined.

7.2 Deformation of Droplet Under Shear Flow. We simulate the droplet deformation under shear flow. A single droplet Ω_1 in an ambient fluid Ω_2 between two parallel plates is

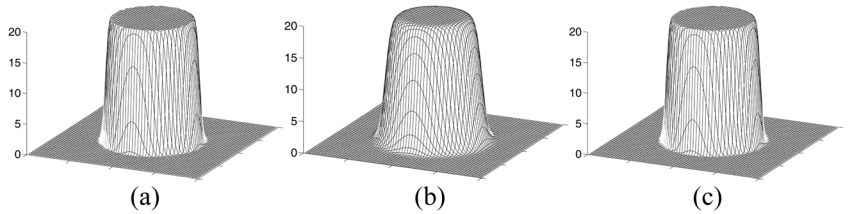

Fig. 10 Numerical pressure field p for (a) LSM, (b) PFM, and (c) IBM

Table 1 Pressure difference $[p]_h$ with $\sigma = 5$ and $r = 0.25$ for different mesh sizes

Mesh	32×32	64×64	128×128
LSM	20.491	20.118	20.057
PFM	17.681	19.441	19.984
IBM	20.066	20.035	20.020

schematically depicted in Fig. 11. The shear flow is generated by the Dirichlet boundary condition $\mathbf{u} = (\pm\dot{\gamma}y, 0)$ at the top and bottom boundary, where $\dot{\gamma}$ is the shear rate. We use the periodic condition for the x-direction.

We consider the density and viscosity ratios of the droplet to ambient fluid to have unit values and neglect the influence of the gravitational force. This problem is nondimensionalized by the undeformed droplet radius R. We define the Reynolds number $\mathrm{Re} = \rho_2 R^2\dot{\gamma}/\eta_2$ and capillary number $\mathrm{Ca} = \eta_2 R\dot{\gamma}/\sigma$. The Weber number can then be written as $\mathrm{We} = \mathrm{Re}\cdot\mathrm{Ca}$. The Navier–Stokes equations (1) and (2) are nondimensionalized as

$$\frac{\partial \mathbf{u}}{\partial t} + \mathbf{u}\cdot\nabla\mathbf{u} = -\nabla p + \frac{1}{\mathrm{Re}}\Delta\mathbf{u} + \frac{1}{\mathrm{We}}\mathbf{SF} \tag{94}$$

$$\nabla\cdot\mathbf{u} = 0 \tag{95}$$

To measure the magnitude of the droplet deformation, we use the Taylor deformation number D, defined as $D = (L-B)/(L+B)$, where L and B are the major and minor droplet semiaxes, shown in Fig. 11.

First, we compare the deformation number of the three methods with the results of Ref. [72]. For the initial state, the droplet radius is $R = 0.5$, centered at $(0,0)$ in the computational domain $\Omega = (-1,1)\times(-1,1)$. The shear rate $\dot{\gamma} = 1$, 32×32 mesh grid, and time step $\Delta t = 0.0005$ are used. For other parameters, $\alpha = h$ is used in LSM, $\varepsilon = 0.07$ and $\mathrm{Pe} = 1/\varepsilon$ are used in PFM, and $N = 402$ is used in IBM. Figure 12 shows the deformation number with different Re and Ca numbers. The results are in a good agreement with those studied in Ref. [72].

Next, we compare the results of the three methods by the long evolution. For the initial state, the droplet radius is $R = 0.5$ and its center is $(0,0)$ in $\Omega = (-2,2)\times(-1,1)$. We take the other parameters as: $\mathrm{Re} = 5$, $\mathrm{Ca} = 0.6$, and $\dot{\gamma} = 1$. The 256×128 mesh grid and time step $\Delta t = 0.0002$ are used. For LSM, the parameter $\alpha = 3h$ is used. For PFM, a Peclet number $Pe = 0.1/\varepsilon$ and $\varepsilon = 0.06$ are used. For IBM, we fix the number of Lagrangian marker points as 1000. Figure 13(*a*) shows that the droplet shapes at the time $t = 8$. These shapes are in qualitative agreement for each result. We also plot the deformation number D with the time t in Fig. 13(*b*). The difference between the curves for all methods is small at all times.

7.3 Simulation of the Falling Droplet. Simulating a falling droplet is a classical test problem in two-phase flows. We demonstrate the adaptability of the three methods by simulating a falling droplet Ω_1 surrounded by the ambient fluid Ω_2 under a gravitational force. We use the periodic and zero Dirichlet boundary conditions for the x- and y-directions of velocity field, respectively.

We nondimensionalize the governing equation based on the properties of the ambient fluid, including the dimensionless parameters, Reynolds number $\mathrm{Re} = \rho_2 U_c L_c/\eta_2$, Weber number $\mathrm{We} = \rho_2 U_c^2 L_c/\sigma$, and Froude number $\mathrm{Fr} = U_c^2/(gL_c)$, where U_c is the characteristic velocity, L_c is the characteristic length, and ρ_2, η_2 are the density and viscosity of the ambient fluid, respectively. We consider the viscosity ratio of the droplet and ambient fluid to have the unit value. The nondimensionalized Navier–Stokes equations (1) and (2) can be written as

$$\rho\left(\frac{\partial \mathbf{u}}{\partial t} + \mathbf{u}\cdot\nabla\mathbf{u}\right) = -\nabla p + \frac{1}{\mathrm{Re}}\Delta\mathbf{u} + \frac{1}{We}\mathbf{SF} + \frac{\rho}{Fr}\mathbf{g} \tag{96}$$

$$\nabla\cdot\mathbf{u} = 0 \tag{97}$$

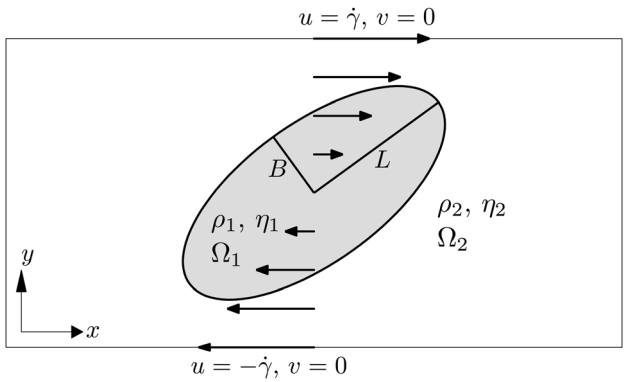

Fig. 11 Schematic illustration of droplet deformation under shear flow

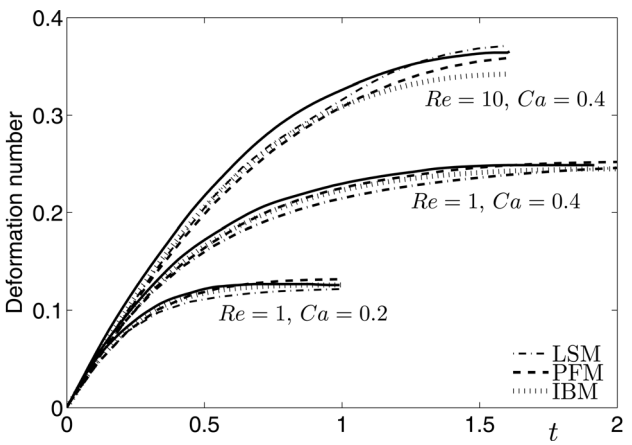

Fig. 12 Deformation number D as a function of time t comparing with results (solid lines) in Ref. [72]

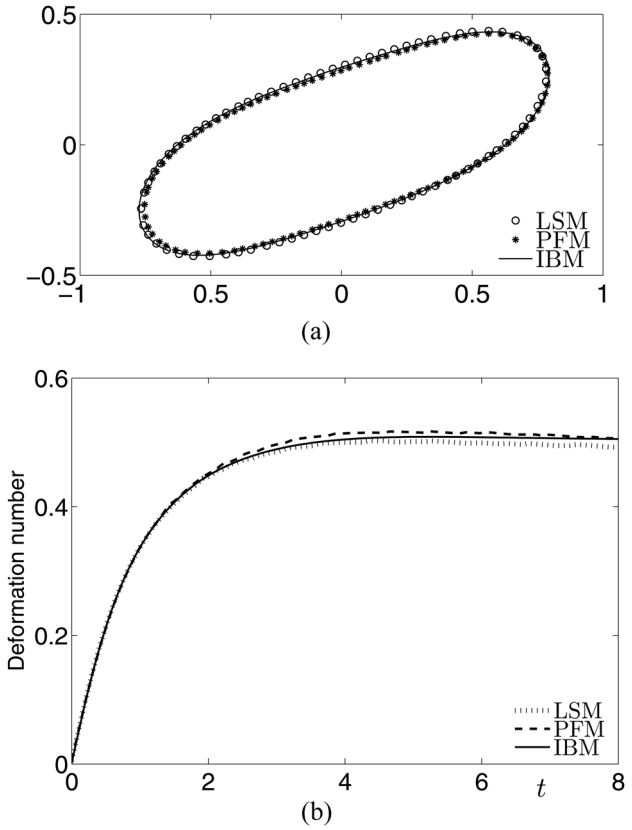

Fig. 13 (*a*) Interfaces of the three methods and (*b*) Deformation numbers as a function of time.

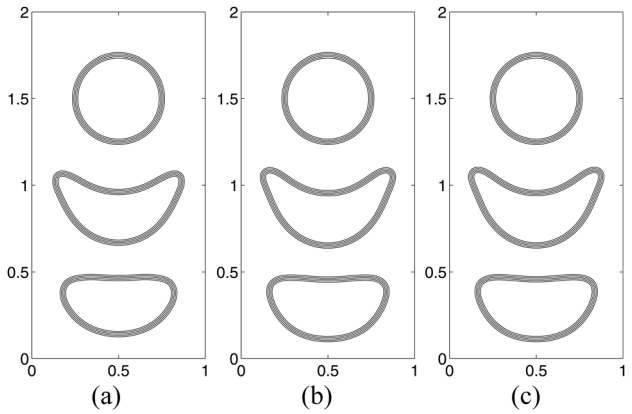

Fig. 14 Evolution of the droplet using different interfacial thickness parameter (*a*) $\alpha = 0.5h$, (*b*) $\alpha = h$, and (*c*) $\alpha = 2h$ in LSM. The contours are drawn at times $t = 0$, 2.5, and 4.5 from top to bottom. Contour levels are $-2h$, $-h$, 0, h, and $2h$.

We set the droplet density to $\rho_1 = 3$ and ambient fluid density to $\rho_2 = 1$. We consider a circular droplet with radius $R = 0.25$ centered at $(0.5, 1.5)$ in the computational domain $\Omega = (0,1) \times (0,2)$. We take the characteristic parameters as $U_c = L_c = 1$, and set $\sigma = 0.04$ and $\eta_1 = \eta_2 = 0.01$, then the dimensionless parameter values are $\mathrm{Re} = 100$, $\mathrm{We} = 25$, and $Fr = 1/g$. The gravitational force is set to $\mathbf{g} = (0, -1)$. The 128×256 mesh grid, space step $h = 1/64$, and time step $\Delta t = 0.0002$ are used. We consider the effect of the gravitational force together with the relatively small interfacial tension.

In LSM, the parameter α in the smoothed Heaviside function determines the interfacial thickness for the transition of fluid properties. An appropriate value of α will give a reasonable droplet

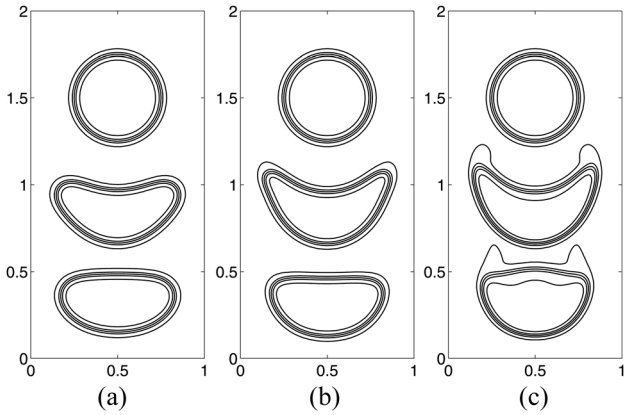

Fig. 15 Evolution of the droplet using different Peclet number (*a*) $Pe = 0.1/\varepsilon$, (*b*) $Pe = 1/\varepsilon$, and (*c*) $Pe = 10/\varepsilon$ in PFM. The contours are drawn at times $t = 0$, 2.5, and 4.5 from top to bottom. Contour levels are -0.9, -0.45, 0, 0.45, and 0.9.

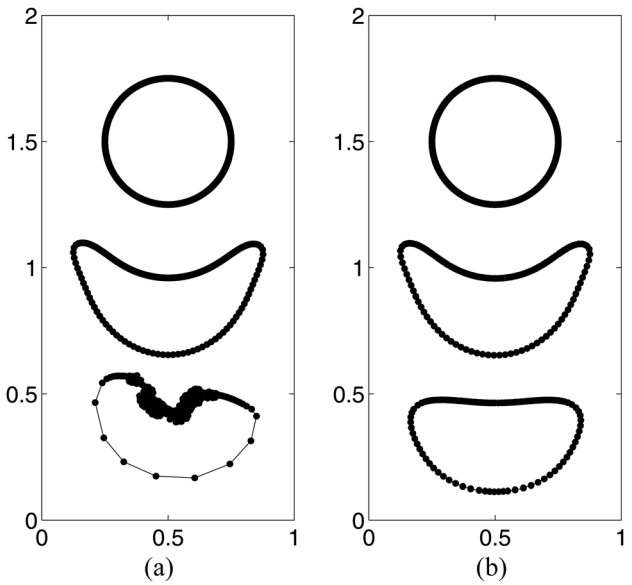

Fig. 16 Evolution of the droplet in IBM (*a*) without and (*b*) with deletion and addition procedures. The marker points are drawn at times $t = 0$, 2.5, and 4.5 from top to bottom.

evolution. Figure 14 shows the evolution of the droplet shape for different values of α. For a narrow interface $\alpha = 0.5h$, the droplet shrinks compared to those of the other parameters $\alpha = h$ and $2h$. It can also be seen that there is no evident shape difference for larger values of $\alpha = h$, $2h$. Our comparison can suggest that $\alpha = 1.5h$ is accurate enough.

In PFM, the Peclet number plays an important role in the interface evolution. To investigate the effect of the Peclet number and determine an appropriate value, we consider three different Peclet numbers $Pe = 0.1/\varepsilon$, $1/\varepsilon$, and $10/\varepsilon$, where $\varepsilon = 4h/[2\sqrt{2}\tan^{-1}(0.9)]$. The droplet contours at different times and Peclet numbers are shown in Fig. 15. The droplet shape is flatter in the case of $Pe = 0.1/\varepsilon$, while the diffuse interface is smeared out or compressed in the case of $Pe = 10/\varepsilon$. These could lead to inaccurate and nonphysical results. Compared with the results of LSM, $Pe = 1/\varepsilon$ is a better choice.

In IBM, we consider the effect of the distribution of marker points on the evolution of droplet. The initial marker points are evenly distributed as follows: Let N be the nearest integer number of $2\pi Rm/h$, where m is an integer. Δs_l is approximately taken as

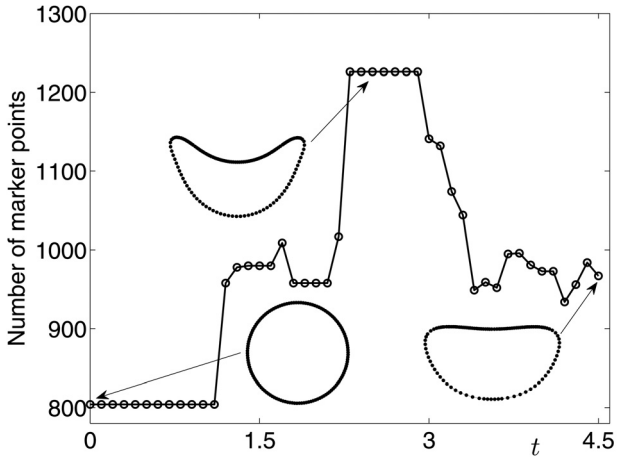

Fig. 17 Variation of the number of marker points as a function of time in case of Fig. 16(*b*)

h/m. We use a moderate number $m = 4$ and, therefore, $N = 804$ for the initial droplet. Figure 16(*a*) shows the time evolution of droplet shape with a fixed number N. Note that Δs_l is varied by the flow field. The droplet shape is well maintained up to $t = 2.5$, but marker points become concentrated at $t = 4.5$, making the connected line heavily intertwined and eventually leading to a collapse of the droplet shape. To overcome this problem, we adaptively add and delete marker points so that $0.1h < \Delta s_l < 0.5h$. Figure 16(*b*) shows the evolution of droplet shape with the deletion and addition procedures. The number of marker points as a function of time is shown in Fig. 17. The interface points are more evenly distributed and the droplet shape remains good at $t = 4.5$ in Fig. 16(*b*).

Finally, we compare the droplet evolution using the optimal strategy of each method. Figure 18 shows a comparison of the droplet shape at time $t = 0$, 2.5, and 4.5 for three methods. As shown in the figure, the droplet shapes are well matched at each time, demonstrating their strong ability for accurate interfacial representation.

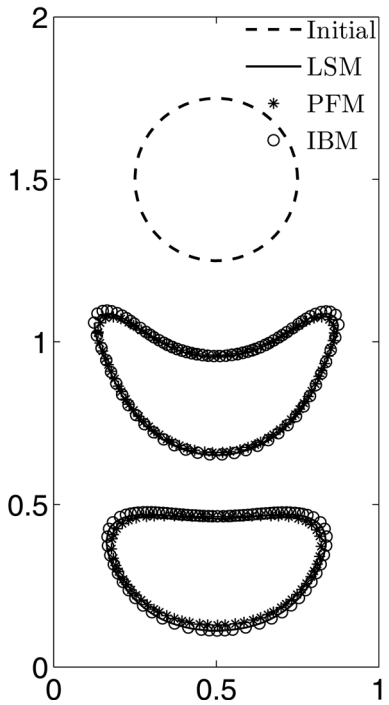

Fig. 18 Comparison of the falling droplet for the three methods with optimal parameters at time $t = 0$, 2.5, and 4.5

Table 2 CPU times (s) for the shear flow and falling droplet simulations. The calculations are run to the time $t = 3$.

Case	LSM	PFM	IBM
Shear flow	2018	2849	421
Falling droplet	2320	4538	3234

7.4 Computational Cost. We compare the computational cost of the shear flow and falling droplet simulations for each method. The initial conditions and parameters follow those of Figs. 13 and 18. Table 2 lists the central processing unit (CPU) time of each method for calculating up to time $t = 3$. We can see that IBM has less computational cost than the other two methods in the shear flow simulation. In this case, LSM and PFM have additional computational costs such as the reinitialization and Cahn–Hilliard equations. For the falling droplet test, the necessity of solving an indicator function and redistributing marker points by adding and deleting points accounts for the rapid CPU time increment for IBM. Therefore, the CPU time cost of each method is case by case, and the three methods have more or less similar computational expense.

8 Discussion and Conclusions

From the numerical point of view, the three methods we have described belong to the "diffuse interface" model because of the use of the δ function. The smeared-out interface by the δ function is in favor of computation of surface tension and fluid properties even if it is a real sharp interface in the physical problems. For the presentation of interface, there is a finite width for the phase-field method, but it is "zero" width for the level set and immersed boundary methods. Meanwhile, the interface is implicitly expressed by the level set and phase-field methods and explicitly by the immersed boundary method.

Because the interface is represented by an implicit level set function, there is no need for special consideration of complex interfacial topology changes with separation and merging. For the level set method using reinitialization technique, the accuracy and efficiency are greatly determined by that of reinitialization procedure, and mass loss is a problem for the original level set method. For the phase-field method, it shares the advantages with the level set method that there is no need for tracking the interface explicitly. In the Cahn–Hilliard type phase-field model, we need to carefully select the Peclet number to make interface evolution reasonable, and an appropriate interface width is also needed. For the immersed boundary method, interface can be represented accurately and explicitly by using a great number of Lagrangian marker points. However, the distribution of marker points must be carefully considered in case nonphysical or undesirable phenomena occur.

In this paper, we applied the level set, phase-field, and immersed boundary methods to the computation of two-phase flows governed by the incompressible and immiscible Navier–Stokes equations. We explained the numerical discretization of each method, introduced their essential concepts, and discussed the strengths and weaknesses. We then performed a series of numerical experiments using each method. Using a pressure difference experiment, we validated each of the algorithms, showing that the numerical solutions are qualitatively in agreement with the theoretical value. By simulating the droplet deformation under a shear flow, the three methods were preliminarily verified. Finally, in the challenging simulation of a falling droplet, we discussed in detail the effects of different parameter values on the evolution of the droplet. CPU time cost was also considered in two simulations to compare the efficiency of each method. The

results agreed reasonably well, demonstrating the ability of all three methods to capture the interface of two-phase flows.

Acknowledgment

The corresponding author (J.S. Kim) was supported by the Ministry of Science, ICT & Future Planning (MSIP) (NRF-2011-0023794). The authors are grateful to the anonymous referees whose valuable suggestions and comments significantly improved the quality of this paper.

References

[1] Caboussat, A., 2005, "Numerical Simulation of Two-Phase Free Surface Flows," Arch. Comput. Method Eng., **12**, pp. 165–224.
[2] Prosperetti, A., and Tryggvason, G., 2007, *Computational Methods for Multiphase Flow*, Cambridge University Press, New York.
[3] Clayton, T. C., Schwarzkopf, J. D., Sommerfeld, M., and Tsuji, Y., 2011, *Multiphase Flows With Droplets and Particles*, CRC Press, Boca Raton, FL.
[4] Worner, M., 2012, "Numerical Modeling of Multiphase Flows in Microfluidics and Micro Process Engineering: A Review of Methods and Applications," Microfluid. Nanofluid., **12**, pp. 841–886.
[5] Brackbill, J. U., Kothe, D. B., and Zemach, C., 1992, "A Continuum Method for Modeling Surface Tension," J. Comput. Phys., **100**, pp. 335–354.
[6] Osher, S., and Sethian, J. A., 1988, "Fronts Propagating With Curvature Dependent Speed: Algorithms Based on Hamilton-Jacobi Formulations," J. Comput. Phys., **79**, pp. 12–49.
[7] Shu, C.-W., and Osher, S., 1988, "Efficient Implementation of Essentially Non-Oscillatory Shock Capturing Schemes," J. Comput. Phys., **77**, pp. 439–471.
[8] Sussman, M., Smereka, P., and Osher, S., 1994, "A Level Set Approach for Computing Solutions to Incompressible Two-Phase Flow," J. Comput. Phys., **114**, pp. 146–159.
[9] Chang, Y. C., Hou, T. Y., Merriman, B., and Osher, S., 1996, "A Level Set Formulation of Eulerian Interface Capturing Methods for Incompressible Fluid Flows," J. Comput. Phys., **124**, pp. 449–464.
[10] Sussman, M., Fatemi, E., Smerekc, P., and Osher, S., 1998, "An Improved Level Set Method for Incompressible Two-Phase Flows," Comput. Fluids, **27** pp. 663–680.
[11] Sethian, J. A., 1999, *Level-Set Methods and Fast Marching Methods: Evolving Interfaces in Computational Geometry, Fluid Mechanics, Computer Vision and Materials Science*, Cambridge University Press, New York.
[12] Sussman, M., Almgren, A., Bell, J., Colella, P., Howell, L. H., and Welcome, M., 1999, "An Adaptive Level Set Approach for Incompressible Two-Phase Flows," J. Comput. Phys., **148**, pp. 81–124.
[13] Sussman, M., and Puckett, E. G., 2000, "A Coupled Level Set and Volume-of-Fluid Method for Computing 3D and Axisymmetric Incompressible Two-Phase Flows," J. Comput. Phys., **162**, pp. 301–337.
[14] Kang, M., Fedkiw, R. P., and Liu, X. D., 2000, "A Boundary Condition Capturing Method for Multiphase Incompressible Flow," J. Sci. Comput., **15**, pp. 323–360.
[15] Smith, K. A., Solis, F. J., Tao, L., Thornton, K., and De La Cruz, M. O., 2000, "Domain Growth in Ternary Fluids: A Level Set Approach," Phys. Rev. Lett., **84**, pp. 91v94.
[16] Osher, S., and Fedkiw, R. P., 2001, "Level Set Methods: An Overview and Some Recent Results," J. Comput. Phys., **169**, pp. 463–502.
[17] Enright, D., Fedkiw, R., Ferziger, J., and Mitchell, I., 2002, "A Hybrid Particle Level Set Method for Improved Interface Capturing," J. Comput. Phys., **183**, pp. 83–116.
[18] Smith, K. A., Solis, F. J., and Chopp, D. L., 2002, "A Projection Method for Motion of Triple Junctions by Level Sets," Interfaces Free Bound., **4**, pp. 263–276.
[19] Osher, S., and Fedkiw, R. P., 2003, *Level Set Methods and Dynamic Implicit Surfaces*, Springer-Verlag, New York.
[20] Sethian, J. A., and Smereka, P., 2003, "Level Set Methods for Fluid Interfaces," Annu. Rev. Fluid Mech., **35**, pp. 341–372.
[21] Xu, J.-J., and Zhao, H.-K., 2003, "An Eulerian Formulation for Solving Partial Differential Equations Along a Moving Interface," J. Sci. Comput., **19**, pp. 573–594.
[22] Sussman, M., 2003, "A Second Order Coupled Level Set and Volume-of-Fluid Method for Computing Growth and Collapse of Vapor Bubbles," J. Comput. Phys., **187**, pp. 110–136.
[23] Smith, K. A., Ottino, J. M., and de la Cruz, M. O., 2004, "Encapsulated Drop Breakup in Shear Flow," Phys. Rev. Lett., **93**, pp. 204501-1–204501-4.
[24] Olsson, E., and Kreiss, G., 2005, "A Conservative Level Set Method for Two Phase Flow,'' J. Comput. Phys., **210**, pp. 225–246.
[25] Majumder, S., and Chakraborty, S., 2005, "New Physically Based Approach of Mass Conservation Correction in Level Set Formulation for Incompressible Two-Phase Flows," ASME J. Fluids Eng., **127**, pp. 554–563.
[26] Tanguy, S., and Berlemont, A., 2005, "Application of a Level Set Method for Simulation of Droplet Collisions," Int. J. Multiphase Flow, **31**, pp. 1015–1035.
[27] Enright, D., Losasso, F., and Fedkiw, R., 2005, "A Fast and Accurate Semi-Lagrangian Particle Level Set Method," Comput. Struct., **83**, pp. 479–490.
[28] Shepel, S. V., and Smith, B. L., 2006, "New Finite-Element/Finite-Volume Level Set Formulation for Modelling Two-Phase Incompressible Flows," J. Comput. Phys., **218**, pp. 479–494.
[29] Grooss, J., and Hesthaven, J. S., 2006, "A Level Set Discontinuous Galerkin Method for Free Surface Flows," Comput. Meth. Appl. Mech. Eng., **195**, pp. 3406–3429.
[30] Hong, J. M., Shinar, T., Kang, M., and Fedkiw, R., 2007, "On Boundary Condition Capturing for Multiphase Interfaces," J. Sci. Comput., **31**, pp. 99–125.
[31] Olsson, E., Kreiss, G., and Zahedi, S., 2007, "A Conservative Level Set Method for Two Phase Flow II," J. Comput. Phys., **225**, pp. 785–807.
[32] Sussman, M., Smith, K. M., Hussaini, M. Y., Ohta, M., and Zhi-Wei, R., 2007, "A Sharp Interface Method for Incompressible Two-Phase Flows," J. Comput. Phys., **221**, pp. 469–505.
[33] Croce, R., Griebel, M., and Schweitzer, M. A., 2010, "Numerical Simulation of Bubble and Droplet Deformation by a Level Set Approach With Surface Tension in Three Dimensions," Int. J. Numer. Meth. Fluids, **62**, pp. 963–993.
[34] Ausas, R. F., Dari, E. A., and Buscaglia, G. C., 2011, "A Geometric Mass-Preserving Redistancing Scheme for the Level Set Function," Int. J. Numer. Meth. Fluids, **65**, pp. 989–1010.
[35] Pathak, M., 2012, "Numerical Analysis of Droplet Dynamics Under Different Temperature and Cross-Flow Velocity Conditions," ASME J. Fluids Eng., **134**, pp. 044501-1–044501-6.
[36] Starovoitov, V. N., 1994, "Model of the Motion of a Two-Component Liquid With Allowance of Capillary Forces," J. Appl. Mech. Tech. Phys., **35**, pp. 891–897.
[37] Chella, R., and Viñals, J., 1996, "Mixing of a Two-Phase Fluid by Cavity Flow," Phys. Rev. E, **53**, pp. 3832–3840.
[38] Gurtin, M. E., Polignone, D., and Vinals, J., 1996, "Two-Phase Binary Fluids and Immiscible Fluids Described by an Order Parameter," Math. Models Methods Appl. Sci., **6**, pp. 815–831.
[39] Anderson, D. M., McFadden, G. B., and Wheeler, A. A., 1998, "Diffuse-Interface Methods in Fluid Mechanics," Annu. Rev. Fluid Mech., **30**, pp. 139–165.
[40] Lowengrub, J., and Truskinovsky, L., 1998, "Quasi-Incompressible Cahn–Hilliard Fluids and Topological Transitions," Proc. Roy. Soc. London Ser. A, **454**, pp. 2617–2654.
[41] Jacqmin, D., 1999, "Calculation of Two-Phase Navier–Stokes Flows Using Phase-Field Modeling," J. Comput. Phys., **155**, pp. 96–127.
[42] Jacqmin, D., 2000, "Contact-Line Dynamics of a Diffuse Fluid Interface," J. Fluid Mech., **402**, pp. 57–88.
[43] Verschueren, M., Van de Vosse, F. N., and Meijer, H. E. H., 2001, "Diffuse-Interface Modelling of Thermocapillary Flow Instabilities in a Hele-Shaw Cell," J. Fluid Mech., **434**, pp. 153–166.
[44] Lee, H.-G., Lowengrub, J. S., and Goodman, J., 2002, "Modeling Pinchoff and Reconnection in a Hele-Shaw Cell. I. The Models and Their Calibration," Phys. Fluids, **14**, pp. 492–513.
[45] Lee, H.-G., Lowengrub, J. S., and Goodman, J., 2002, "Modeling Pinchoff and Reconnection in a Hele-Shaw Cell. II. Analysis and Simulation in the Nonlinear Regime," Phys. Fluids, **14**, pp. 514–545.
[46] Boyer, F., 2002, "A Theoretical and Numerical Model for the Study of Incompressible Mixture Flows," Comput. Fluids, **31**, pp. 41–68.
[47] Badalassi, V. E., Ceniceros, H. D., and Banerjee, S., 2003, "Computation of Multiphase Systems With Phase Field Models," J. Comput. Phys., **190**, pp. 371–397.
[48] Liu, C., and Shen, J., 2003, "A Phase Field Model for the Mixture of Two Incompressible Fluids and Its Approximation by a Fourier-Spectral Method," Phys. D, **179**, pp. 211–228.
[49] Kim, J., Kang, K., and Lowengrub, J., 2004, "Conservative Multigrid Methods for Cahn-Hilliard Fluids," J. Comput. Phys., **193**, pp. 511–543.
[50] Sun, Y., and Beckermann, C., 2004, "Diffuse Interface Modeling of Two-Phase Flows Based on Averaging: Mass and Momentum Equations," Phys. D, **198**, pp. 281–308.
[51] Khatavkar, V. V., Anderson, P. D., Duineveld, P. C., and Meijer, H. H. E., 2005, "Diffuse Interface Modeling of Droplet Impact on a Pre-Patterned Solid Surface," Macromol. Rapid Commun., **26**, pp. 298–303.
[52] Kim, J., 2005, "A Diffuse-Interface Model for Axisymmetric Immiscible Two-Phase Flow," Appl. Math. Comput., **160**, pp. 589–606.
[53] Yue, P., Feng, J. J., Liu, C., and Shen, J., 2005, "Diffuse-Interface Simulations of Drop Coalescence and Retraction in Viscoelastic Fluids," J. Non-Newton. Fluid Mech., **129**, pp. 163–176.
[54] Kim, J., 2005, "A Continuous Surface Tension Force Formulation for Diffuse-Interface Models," J. Comput. Phys., **204**, pp. 784–804.
[55] Badalassi, V. E., and Banerjee, S., 2005, "Nano-Structure Computation With Coupled Momentum Phase Ordering Kinetics Models," Nucl. Eng. Des., **235**, pp. 1107–1115.
[56] Yang, X., Feng, J. J., Liu, C., and Shen, J., 2006, "Numerical Simulations of Jet Pinching-Off and Drop Formation Using an Energetic Variational Phase-Field Method," J. Comput. Phys., **218**, pp. 417–428.
[57] Yue, P., Zhou, C., and Feng, J. J., 2007, "Spontaneous Shrinkage of Drops and Mass Conservation in Phase-Field Simulations," J. Comput. Phys., **223**, pp. 1–9.
[58] Ding, H., and Spelt, P. D. M., 2007, "Wetting Condition in Diffuse Interface Simulations of Contact Line Motion," Phys. Rev. E, **75**, p. 046708.
[59] Khatavkar, V. V., Anderson, P. D., Duineveld, P. C., and Meijer, H. H. E., 2007, "Diffuse-Interface Modelling of Droplet Impact," J. Fluid Mech., **581**, pp. 97–127.

[60] He, Q., and Kasagi, N., 2008, "Phase-Field Simulation of Small Capillary-Number Two-Phase Flow in a Microtube," Fluid Dyn. Res., **40**, pp. 497–509.
[61] Kim, J., 2009, "A Generalized Continuous Surface Tension Force Formulation for Phase-Field Models for Multi-Component Immiscible Fluid Flows," Comput. Methods Appl. Mech. Eng., **198**, pp. 3105–3112.
[62] Shen, J., and Yang, X., 2009, "An Efficient Moving Mesh Spectral Method for the Phase-Field Model of Two-Phase Flows," J. Comput. Phys., **228**, pp. 2978–2992.
[63] Acar, R., 2009, "Simulation of Interface Dynamics: A Diffuse-Interface Model," Visual Comput., **25**, pp. 101–115.
[64] Ceniceros, H. D., Nós, R. L., and Roma, A. M., 2010, "Three-Dimensional, Fully Adaptive Simulations of Phase-Field Fluid Models," J. Comput. Phys., **229**, pp. 6135–6155.
[65] Chiu, P. H., and Lin, Y. T., 2011, "A Conservative Phase Field Method for Solving Incompressible Two-Phase Flows," J. Comput. Phys., **230**, pp. 185–204.
[66] Kim, J., 2012, "Phase-Field Models for Multi-Component Fluid Flows," Commun. Comput. Phys., **12**, pp. 613–661.
[67] Lee, H. G., Choi, J. W., and Kim, J., 2012, "A Practically Unconditionally Gradient Stable Scheme for the N-Component Cahn–Hilliard System," Physica A, **391**, pp. 1009–1019.
[68] Peskin, C. S., 1977, "Numerical Analysis of Blood Flow in the Heart," J. Comput. Phys., **25**, pp. 220–252.
[69] Peskin, C. S., and McQueen, D. M., 1980, "Modeling Prosthetic Heart Valves for Numerical Analysis of Blood Flow in the Heart," J. Comput. Phys., **37**, pp. 113–132.
[70] Unverdi, S. O., and Tryggvason, G. 1992, "A Front-Tracking Method for Viscous, Incompressible, Multi-Fluid Flows," J. Comput. Phys., **100**, pp. 25–37.
[71] Peskin, C. S., and Printz, B. F., 1993, "Improved Volume Conservation in the Computation of Flows With Immersed Elastic Boundaries," J. Comput. Phys., **105**, pp. 33–46.
[72] Sheth, K. S., and Pozrikidis, C., 1995, "Effects of Inertia on the Deformation of Liquid Drops in Simple Shear Flow," Comput. Fluids, **24**, pp. 101–119.
[73] Stockie, J. M., 1997, "Analysis and Computation of Immersed Boundaries, With Application to Pulp Fibres," Ph.D. thesis, University of British Columbia, British Columbia, Canada.
[74] Udaykumar, H. S., Kan, H. C., Shyy, W., and Tran-Son-Tay, R., 1997, "Multiphase Dynamics in Arbitrary Geometries on Fixed Cartesian Grids," J. Comput. Phys., **137**, pp. 366–405.
[75] Kan, H. C., Udaykumar, H. S., Shyy, W., and Tran-Son-Tay, R., 1998, "Hydrodynamics of a Compound Drop With Application to Leukocyte Modeling," Phys. Fluids., **10**, pp. 760–774.
[76] Roma, A. M., Peskin, C. S., and Berger, M. J., 1999, "An Adaptive Version of the Immersed Boundary Method," J. Comput. Phys., **153**, pp. 509–534.
[77] Kan, H. C., Shyy, W., Udaykumar, H. S., Vigneron, P., and Tran-Son-Tay, R., 1999, "Effects of Nucleus on Leukocyte Recovery," Ann. Biomed. Eng., **27**, pp. 648–655.
[78] Peskin, C. S., 2002, "The Immersed Boundary Method," Acta Numer., **11**, pp. 479–517.
[79] Francois, M., and Shyy, W., 2003, "Computations of Drop Dynamics With the Immersed Boundary Method, Part 1: Numerical Algorithm and Buoyancy-Induced Effect," Numer. Heat Tran. B, **44**, pp. 101–118.
[80] Francois, M., Uzgoren, E., Jackson, J., and Shyy, W., 2004, "Multigrid Computations With the Immersed Boundary Technique for Multiphase Flows," Int. J. Numer. Meth. Heat Fluid Flow, **14**, pp. 98–115.
[81] Mittal, R., and Iaccrino, G., 2005, "Immersed Boundary Methods," Annu. Rev. Fluid Mech., **37**, pp. 239–261.
[82] Uhlmann, M., 2005, "An Immersed Boundary Method With Direct Forcing for the Simulation of Particulate Flows," J. Comput. Phys., **209**, pp. 448–476.
[83] Griffith, B. E., and Peskin, C. S., 2005, "On the Order of Accuracy of the Immersed Boundary Method: Higher Order Convergence Rates for Sufficiently Smooth Problems," J. Comput. Phys., **208**, pp. 75–105.
[84] Griffith, B. E., Hornung, R. D., McQueen, D. M., and Peskin, C. S., 2005, "An Adaptive, Formally Second Order Accurate Version of the Immersed Boundary Method," J. Comput. Phys., **223**, pp. 10–49.
[85] Newren, E., Fogelson, A. L., Guy, R. D., and Kirby, R. M., 2007, "Unconditionally Stable Discretizations of the Immersed Boundary Equations," J. Comput. Phys., **222**, pp. 702–719.
[86] Shin, S. J., Huang, W.-X., and Sung, H. J., 2008, "Assessment of Regularized Delta Functions and Feedback Forcing Schemes for an Immersed Boundary Method," Int. J. Numer. Meth. Fluids, **58**, pp. 263–286.
[87] Kim, Y., and Peskin, C. S., 2008, "Numerical Study of Incompressible Fluid Dynamics With Nonuniform Density by the Immersed Boundary Method," Phys. Fluids, **20**, p. 062101.
[88] Yang, X., Zhang, X., Li, Z., and He, G.-W., 2009, "A Smoothing Technique for Discrete Delta Functions With Application to Immersed Boundary Method in Moving Boundary Simulations," J. Comput. Phys., **228**, pp. 7821–7836.
[89] Chen, K. Y., Feng, K. A., Kim, Y., and Lai, M. C., 2011, "A Note on Pressure Accuracy in Immersed Boundary Method for Stokes Flow," J. Comput. Phys., **230**, pp. 4377–4383.
[90] Li, Y., Jung, E., Lee, W., Lee, H. G., and Kim, J., 2012, "Volume Preserving Immersed Boundary Methods for Two-Phase Fluid Flows," Int. J. Numer. Methods Fluids, **69**, pp. 842–858.
[91] Li, Y., Yun, A., Lee, D., Shin, J., Jeong, D., and Kim, J., 2013, "Three-Dimensional Volume-Conserving Immersed Boundary Model for Two-Phase Fluid Flows," Comput. Meth. Appl. Mech. Eng., **257**, pp. 36–46.
[92] Cahn, J. W., and Hilliard, J. E., 1958, "Free Energy of a Nonuniform System. I. Interfacial Free Energy," J. Chem. Phys., **28**, 258–267.
[93] LeVeque, R. J., and Li, Z., 1994, "The Immersed Interface Method for Elliptic Equations With Discontinuous Coefficients and Singular Sources," SIAM J. Numer. Anal., **31**, pp. 1019–1044.
[94] LeVeque, R. J., and Li, Z., 1997, "Immersed Interface Methods for Stokes Flow With Elastic Boundaries or Surface Tension," SIAM J. Sci. Comput., **18**, pp. 709–735.
[95] Berthelsen, P. A., 2004, "A Decomposed Immersed Interface Method for Variable Coefficient Elliptic Equations With Non-Smooth and Discontinuous Solutions," J. Comput. Phys., **197**, pp. 364–386.
[96] Li, Z., Ito, K., and Lai, M. C., 2007, "An Augmented Approach for Stokes Equations With a Discontinuous Viscosity and Singular Forces," Comput. Fluids, **36**, pp. 622–635.
[97] Ye, T., Mittal, R., Udaykumar, H. S., and Shyy, W., 1999, "An Accurate Cartesian Grid Method for Viscous Incompressible Flows With Complex Immersed Boundaries," J. Comput. Phys., **156**, pp. 209–240.
[98] Fadlun, E. A., Verzicco, R., Orlandi, P., and Mohd-Yusof, J., 2000, "Combined Immersed-Boundary Finite-Difference Methods for Three-Dimensional Complex Flow Simulations," J. Comput. Phys., **161**, pp. 35–60.
[99] Deng, J., Shao, X. M., and Ren, A. L., 2006, "A New Modification of the Immersed-Boundary Method for Simulating Flows With Complex Moving Boundaries," Int. J. Numer. Meth. Fluids, **52**, pp. 1195–1213.
[100] Sheu, T. W. H., Ting, H. F., and Lin, R. K., 2008, "An Immersed Boundary Method for the Incompressible Navier–Stokes Equations in Complex Geometry," Int. J. Numer. Meth. Fluids, **56**, pp. 877–898.
[101] Shyam Kumar, M. B., and Vengadesan, S., 2012, "Influence of Rounded Corners on Flow Interference Due to Square Cylinders Using Immersed Boundary Method," ASME J. Fluids Eng., **134**, pp. 091203-1–091203-23.
[102] Harlow, F. H., and Welch, J. E., 1965, "Numerical Calculation of Time-Dependent Viscous Incompressible Flow of Fluid With Free Surface, Phys. Fluids., **8**, pp. 2182–2189.
[103] Chorin, A. J., 1968, "Numerical Solution of the Navier–Stokes Equations," Math. Comput., **22**, pp. 745–762.
[104] Trottenberg, U., Oosterlee, C. W., and Schüller, A., 2001, *Multigrid*, Academic Press, New York.
[105] Eyre, D. J., 1998, "Unconditionally Gradient Stable Time Marching the Cahn–Hilliard Equation," Mater. Res. Soc. Symp. Proc., **529**, pp. 39–46.
[106] Kim, J. S., and Bae, H. O., 2008, "An Unconditionally Gradient Stable Adaptive Mesh Refinement for the Cahn–Hilliard Equation," J. Korean Phys. Soc., **53**, pp. 672–679.